Bachelor Thesis

Reconfigurable Particle Manipulation in Zebrafish Embryos

Julian Luginbühl

Hemin Pan

Adviser

Prof. Dr. Daniel Ahmed
Acoustic Robotics Systems Lab
Swiss Federal Institute of Technology Zurich (ETH)

12-2024

ARSL
Acoustic Robotics Systems Lab

ETH
Eidgenössische Technische Hochschule Zürich
Swiss Federal Institute of Technology Zurich

Preface

I would like to thank Prof. Dr. Daniel Ahmed for giving me the opportunity to write my Bachelor's thesis at the Acoustic Robotics Systems Lab, as well as for his support. In addition, I want to thank the entire ARSL team, especially Hemin Pan, the adviser on this thesis, and Dr. Jingjing Zang of the Institute of Molecular Life Sciences.

Abstract

This thesis explores the potential of using surface acoustic wave (SAW) devices for microparticle manipulation. By leveraging the principles of acoustofluidics and focused Interdigital Transducers (FIDTs), this project aimed to achieve precise trapping and manipulation of particles in the vasculature of zebrafish. Initial *in vitro* experiments characterized the resonance frequencies of FIDTs and simulated blood flow using microfluidic channels. The results showed successful particle trapping at specific frequencies under static and controlled fluid flow conditions.

Subsequent *in vivo* experiments encountered challenges due to higher fluid velocities. Although particle manipulation was successfully demonstrated in larger cavities, achieving reliable trapping in narrow vessels proved to be difficult.

This work demonstrates the feasibility of employing FIDTs for targeted particle manipulation, points out critical challenges in achieving precise *in vivo* control, and proposes future directions, including further device optimization and broader biomedical applications for targeted drug delivery, tumor treatment, and wound healing. Advancing research in this area is crucial, as it holds great potential to enhance biomedical applications.

Contents

List of Tables

List of Figures

Notation

Abbreviations

1D	One-dimensional
2D	Two-dimensional
3D	Three-dimensional
ARF	Acoustic Radiation Force
ACF	Acoustic Contrast Factor
BAW	Bulk Acoustic Waves
DI water	Deionised Water
IDT	Interdigital Transducer
FIDT	Focused Interdigital Transducer
MHz	Megahertz
IPA	Isopropyl Alcohol
PS	Polystyrene
$LiNbO_3$	Lithium Niobate
PDMS	Polydimethylsiloxane
SAW	Surface Acoustic Wave
SSAW	Standing Surface Acoustic Wave
TSAW	Traveling Surface Acoustic Wave
AN	Antinode
PN	Positive node

Symbols

f	Frequency
V_{pp}	Peak-to-Peak Voltage
x	Position
y	Position
z	Position
λ	Wavelength
ρ	Density
μ	Dynamic viscosity
ν	Kinematic viscosity

Key Terms and Notations

In this thesis, the following conventions and definitions are adopted for consistency and clarity:

- **Vectors and Vector Fields**: Represented in boldface type (e.g., $\mathbf{v}$ for velocity vector).
- **Scalars and Scalar Fields**: Denoted in standard characters (e.g., p for pressure).
- **Terminology**: The terms *microfluidic chamber*, *microfluidic channel* and *PDMS channel/chamber* are used interchangeably throughout this thesis, referring to the fabricated structures designed to guide fluid flow in microscale experiments.

Chapter 1

Introduction

Acoustic waves, and specifically ultrasound waves which are high frequency mechanical waves ($\geq$ 20 kHz), have been used in medical applications for many decades now. For the most part, acoustic waves have been used to diagnose, screen, and treat patients. The success of sound-powered devices is attributed to their biocompatible, non-invasive and contactless nature and their compatibility with various visualization techniques [1], [2]. In recent years, advancements in microelectromechanical systems have accelerated developments of new microscale applications, enabling researchers to achieve high-resolution, controllable manipulation of particles, such as cells and other bioparticles [3]. From that many use-cases arise, such as targeted drug delivery, sorting and patterning of bioparticles, tumor treatment, and tissue engineering [2], [4], [5].

1.1 Background Information

One of the technologies for the precise manipulation of bioparticles, which is relevant in the context of this thesis, is acoustic tweezers. This emerging platform enables the precise spatial and temporal manipulation of matter at scales ranging from nanometers to millimeters, achieved through the controlled interaction of sound waves with solids, liquids, and gases. Many of the devices that generate acoustic tweezers are modeled after their predecessor, optical tweezers. Optical tweezers, invented in 1986, were quickly adopted as a tool in biology, chemistry, and physics, and have been used to trap viruses, bacteria, and cells [6], [7]. However, these optical tweezers are less accessible and versatile than acoustic tweezers, because they require high-power lasers, high-numerical aperture objectives, and can be potentially damaging to biological samples. Compared with other platforms for contactless particle manipulation (platforms that rely on magnetic, optoelectronic, plasmonic, electrokinetic or hydrodynamic forces), acoustic tweezers are more versatile and can address many of the limitations of other particle manipulation techniques, including biocompatibility, complexity, and cost [1], [7]. Acoustic tweezers generate well-controlled acoustic pressure profiles using gentle and precise forces on sensitive bio-samples, thus minimizing uninhibited heating and mechanical stresses, which expands the range of applications for acoustic tweezers [4].

Acoustic tweezers are generated by acoustic transducers, which leverage the piezoelectric effect to interconvert mechanical and electrical energy. Specifically, for particle manipulation the inverse piezoelectric effect is employed, as it converts an AC signal into mechanical vibrations. This effect can also be used in the reverse direction for sensing, allowing mechanical deformation to be detected as electrical signals [4], [8].

There are three primary categories of acoustic tweezers: standing-wave tweezers, traveling-wave tweezers and acoustic-streaming tweezers. These can be generated by acoustic wave devices, which produce either bulk acoustic waves (BAWs) or surface acoustic waves (SAWs) [7].

Bulk acoustic waves are a well-developed technology with decades of research and many biomedical applications. In microfluidic devices, BAWs are typically produced by the thickness or transverse vibrations of the piezoelectric transducers [4]. Their manipulation precision is typically lower than that of SAWs because they operate at wavelengths significantly larger than the particles they are intended to manipulate. However, they can handle larger particle clusters and work with higher flow rates than SAWs [7], [9].

Surface acoustic waves are generated by interdigital transducers (IDTs), which are interlocking, ”finger-like” electrodes that excite a piezoelectric substrate to generate mechanical oscillations. The distinguishing feature of SAW devices, in contrast to BAWs, is that acoustic energy is confined to the substrate’s surface, resulting in higher spatial resolution than that typically achieved by BAWs [4], [10].

As mentioned above, there are many applications for acoustic tweezers. Of particular relevance for this thesis is the manipulation of microparticles in zebrafish embryos. Zebrafish are small aquatic vertebrates that are commonly used as a standard model in research [11]. Previous work, presented in *”In vivo acoustic manipulation of microparticles in zebrafish embryo”* [11], demonstrated successful trapping and manipulation of microparticles in the vasculature of zebrafish embryos using BAWs. This study used BAWs to achieve spatial control of microbubbles within the vasculature, suggesting promising applications for drug delivery and biological studies. One major drawback of this approach is the limited operational flexibility of BAW devices, which can only target a single, predefined location in the zebrafish vasculature, thus restricting the effective manipulation radius to approximately 100 μm [11]. Moreover, as already mentioned, BAWs do not provide very high spatial precision. Another study explored the spatially selective manipulation of cells with spiral IDTs. This approach enables the precise targeting and trapping of individual cells within the acoustic field, offering significant potential for applications in microbiology and microrobotics. However, a limitation of this method is its reduced efficiency in capturing and deforming larger clusters of particles, which may restrict its applicability in scenarios requiring manipulation of larger particle accumulations [12].

Building on these findings and addressing the limitations of these previously investigated methods, the aim of this project was to achieve particle manipulation using SAWs generated by FIDTs. Hence, all experiments were conducted exclusively with SAW devices and the subsequent discussions will focus solely on SAWs and SAW-based devices.

1.2 Scope of the Thesis

The primary objective of this bachelor’s thesis, as outlined above, was to investigate the trapping and manipulation of particles in the vasculature of zebrafish embryos and to explore possible applications of this method. Using FIDTs partitioned into four sections, this project aims to overcome some of the limitations identified in previous studies, such as the restricted spatial resolution and flexibility associated with other methods. To achieve this goal, it was necessary first to fabricate and characterize

SAW devices with varying spacings and geometries, as well as microfluidic channels. The objectives of the *in vitro* experiments are the following.

- **IDT characterization:** Accurate determination of resonance frequencies, which reliably generate SAWs with clearly observable particle manipulation (aggregation, patterning, trapping) under static conditions (zero background flow velocity).
- **Robust Particle Manipulation:** Successful and repeatable trapping and deformation of particle clusters with minimal dispersion under simulated fluid flow conditions that closely mimic the vasculature of zebrafish.
- **Successful Manipulation Across Multiple Particle Types:** The aforementioned objectives stated should be consistently achieved across multiple particle types, including polystyrene particles, yeast cells and microbubbles.

These *in vitro* procedures aimed to assess the applicability and effectiveness of the *in vivo* manipulation of particles in zebrafish embryos. The objectives of the subsequent *in vivo* experiments are:

- **Observable Particle Trapping:** Clear visualization of particles trapped at targeted sites within the zebrafish vasculature using FIDTs, effectively counteracting forces induced by high fluid flow velocities.
- **Successful Manipulation Across Multiple Particle Types:** Demonstration of successful and reproducible trapping and deformation of particles and particle clusters within the zebrafish vasculature across multiple particle types, including fluorescent polystyrene particles and fluorescent microbubbles.

The thesis will cover the theoretical background on SAWs and IDTs, as well as the fundamental principles of acoustofluidics. Furthermore, the methodological section details the procedures for characterizing IDTs, as well as the fabrication of both IDTs and microfluidic chambers, and the steps involved in the preparation of the zebrafish experiments. Finally, the experimental results are presented and discussed. To conclude the thesis, potential applications for particle trapping and manipulation in blood vessels will be highlighted, along with proposed strategies for further optimization and refinement of the manipulation of particles in circulatory pathways.

Chapter 2

Theoretical Background

A comprehensive discussion of fluid dynamics, and electronics that is necessary to fully grasp the principles of acoustics and IDTs lies beyond the scope of this thesis. In the following, simplifications will be made for the specific case of our experimental setup.

2.1 Acoustics in Microfluidics

In this chapter, the theory of acoustics in microfluidics is discussed, which explores the interaction of sound waves with fluids, enabling the prediction and control of fluid behavior in small-scale systems. This understanding is essential for the application of particle manipulation.

2.1.1 General Governing Equations

The phenomenon of acoustic streaming can be described quantitatively using fluid dynamics' Continuity equation (conservation of mass) and Navier-Stokes equation (conservation of momentum), while assuming that the fluid is isotropic and homogeneous [13], that is:

$$\frac{\partial \rho}{\partial t} + \nabla \cdot (\rho \mathbf{v}) = 0, \qquad \text{(Continuity)(2.1.1a)}$$

$$\rho \frac{\partial \mathbf{v}}{\partial t} + \rho(\mathbf{v} \cdot \nabla)\mathbf{v} = -\nabla p + \mu \nabla^2 \mathbf{v} + \left(\mu_b + \frac{\mu}{3}\right) \nabla(\nabla \cdot \mathbf{v}) \qquad \text{(Navier-Stokes)(2.1.1b)}$$

Above, $\mathbf{v}$ is the flow velocity, t is the time, p is the fluid pressure, μ and μ_b are the shear and bulk viscosities, respectively[14]. The Continuity equation, Eq. (2.1.1a), states that any change in mass (first term) within a control volume is balanced by the net mass flux (second term) across its boundaries. The Navier-Stokes equation, Eq. (2.1.1b), states that the momentum in a control volume is conserved, where the left side represents the inertia force per unit volume of fluid and the right side describes the net internal forces per unit volume, as body forces are neglected here. The first term on the left side denotes the unsteady acceleration, and the second term represents the convective acceleration. The first term on the right side is the pressure gradient, and the remaining two terms are associated with the viscosity gradients. Together with suitable boundary conditions, these equations can be used to predict fluid motion [15].

There are three types of streaming derived from these equations, shown in Fig. 2.1:
Rayleigh Streaming: Rayleigh streaming describes steady vortical flows generated near boundaries in the presence of standing acoustic waves. This kind of streaming results from the interaction between the oscillating boundary layers and the bulk fluid, leading to circulatory flow [16].
Schlichting Streaming: Schlichting streaming describes the effects on viscous boundary layers adjacent to vibrating surfaces. It characterizes these small-scale vortices that form within the boundary layers as a result of acoustic excitation [17].
Eckart Streaming: Eckart streaming describes the streaming induced by acoustic waves within the bulk fluid. It explains how energy dissipation leads to steady flow patterns throughout the fluid volume [18].

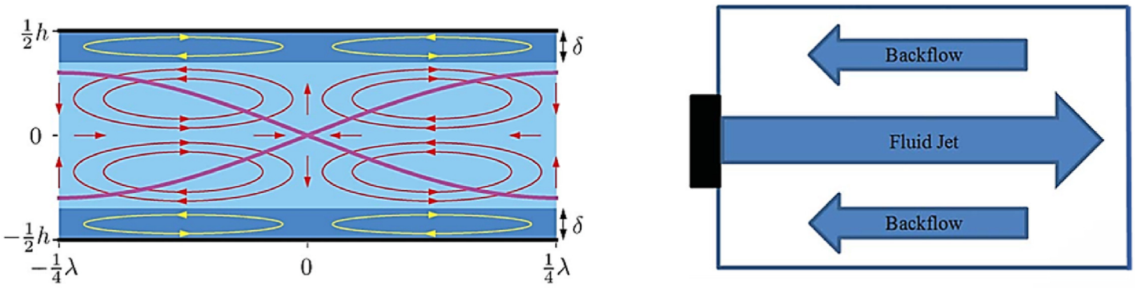

Figure 2.1: Schematic illustration of Rayleigh streaming (indicated by the red ellipses), Schlichting streaming (indicated by the yellow ellipses) and Eckart streaming shown on the right illustration, where the black rectangle represents an acoustic wave transducer [19].

In general, the Navier-Stokes equations are difficult to solve analytically. Therefore, to facilitate tractable analysis, the following sections will introduce simplifications tailored to analyze a special that is reasonable to model the conditions of the experimental setup employed in this thesis.

2.1.2 Simplified Governing Equations

In microfluidic systems, slow streaming with low Reynolds number ($Re << 1$) and thus laminar flow is assumed. These assumptions are valid because the dimensions of the system are very small. The channel dimensions are on the order of micrometers, resulting in small values of characteristic length ($\mathcal{L}$) and velocity (U_0) in the nominator of the Reynolds number expression [11], [15].

$$R_e \equiv \frac{\rho U_0 \mathcal{L}}{\mu}, \tag{2.1.2a}$$

The following derivations for acoustics in microfluidics, applicable to the specific case of the experiments conducted in this thesis, are based on the work presented in *"Acoustofluidics: Theory and Simulation of Radiation Forces at Ultrasound Resonances in Microfluidic Devices"* by Rune Barnkob and Henrik Bruus [20], which rely on the formulation of Gorkov [21].

The setup under consideration, for which the upcoming simplifications are made, consists of a silicon chip affixed to a SAW device using a gel adhesive. The silicon chip contains a microchannel filled with an aqueous particle solution. When applying an AC voltage at a frequency in the MHz range, the IDT vibrates and induces a time-harmonic ultrasound pressure field:

$$p(\mathbf{r},t) = p_1(\mathbf{r})e^{-i\omega t}, \tag{2.1.2b}$$

where $p_1(r)$ represents the spatial amplitude, $\omega = 2\pi f$ is the angular frequency (f is the frequency) and t denotes the time. For simplicity, the time-harmonic factor ($e^{-i\omega}$) is implicitly incorporated, so only the amplitude p_1 is explicitly retained in subsequent expressions.

Assumptions:

- Before the onset of the ultrasound field, the solution is at constant, uniform pressure p_l and zero velocity.
- The influence of the viscosity of the carrier liquid on the forces of acoustic radiation is considered negligible, as the viscous boundary layers are small compared to the wavelength.
- The perturbations in pressure, density, and velocity are small, as they deviate just slightly from ambient conditions, allowing for linearization of the governing equations.

Under these assumptions, a reasonable approximation of the pressure field p_1 and the velocity field $\mathbf{v_1}$ within the microchannel is governed by simple linear acoustics of inviscid fluids. This leads to the Helmholtz wave equation for the pressure field and a potential flow representation for the velocity field.

The Helmholtz wave equation, is derived from the continuity equation (conservation of mass), and Euler's equation (conservation of momentum) and assuming thermal equilibrium. The Helmholtz wave equation is is then given by:

$$\frac{\partial^2 p}{\partial t^2} = c^2\nabla^2 p. \tag{2.1.2c}$$

Substituting in the time-harmonic equation for the pressure field from above, Eq. (2.1.2b), and simplifying yields the following:

$$\nabla^2 p_1 = -\frac{\omega^2}{c_l^2}p_1. \tag{2.1.2d}$$

In the context of potential flow theory, the velocity field $\mathbf{v_1}$ is expressed in general as:

$$\mathbf{v} = \nabla\phi, \tag{2.1.2e}$$

where ϕ is a scalar potential function. As stated above, by considering small perturbations in the velocity and pressure fields, denoted as $\mathbf{v_1}$ and p_1 respectively, and assuming time-harmonic dependence, these perturbations are expressed as:

$$\mathbf{v}_1(\mathbf{r},t) = \mathbf{v}_1(\mathbf{r})e^{-i\omega t}, \quad p_1(\mathbf{r},t) = p_1(\mathbf{r})e^{-i\omega t}, \tag{2.1.2f}$$

Substituting these expressions into Euler's equation:

$$\rho_l \frac{\partial \mathbf{v}_1}{\partial t} = -\nabla p_1, \tag{2.1.2g}$$

and solving for $\mathbf{v_1}$, yields:

$$\mathbf{v}_1 = -\frac{i}{\omega \rho_l} \nabla p_1. \tag{2.1.2h}$$

Comparing equations (2.1.2e) and (2.1.2h) confirms, that $\mathbf{v_1}$ is consistent with potential flow theory.
In our model, the two governing equations can thus be expressed as:

$$\nabla^2 p_1 = -\frac{\omega^2}{c_l^2} p_1. \tag{2.1.2i}$$

$$\mathbf{v}_1 = -\frac{i}{\omega \rho_l} \nabla p_1. \tag{2.1.2j}$$

Above, c_l is the speed of sound and ρ_l is the density of the carrier liquid. The boundary is defined by the surface normal vector $\boldsymbol{n}$. At the boundary of the microchannel, the following boundary conditions are applied [20]:

- **Hard Wall (Rigid Boundary):** Normal velocity component is zero.

$$\mathbf{n} \cdot \mathbf{v}_1 = 0 \implies \mathbf{n} \cdot \nabla p_1 = 0 \tag{2.1.2k}$$

- **Soft Wall (Pressure Release Boundary):** Pressure perturbation is zero.

$$p_1 = 0 \tag{2.1.2l}$$

- **Interface Between Two Media:** Continuity of pressure and normal velocity.

$$p_1^{(a)} = p_1^{(b)}, \quad \frac{1}{\rho_a} \mathbf{n} \cdot \nabla p_1^{(a)} = \frac{1}{\rho_b} \mathbf{n} \cdot \nabla p_1^{(b)} \tag{2.1.2m}$$

2.1.3 Acoustic Resonances

The silicon chamber, as previously described, represents an acoustically hard cavity enclosing the acoustically soft liquid inside the chamber. This leads to acoustic resonances for specific frequencies ω_j, for $j = 1, 2, 3, \ldots$. A resonance frequency ω_j is induced when the average acoustic energy density inside the chamber becomes several orders of magnitude higher than at other frequencies. The resonance frequency depends on the cavity's geometry and the material properties of the entire set-up. In particular, the speed of sound in the medium and the densities of the materials play critical roles. In the general case, the resonance frequencies can only be calculated by applying numerical methods.

However, when assuming that the enclosing material is infinitely hard, the velocity at the wall is zero. In this case, the hard-wall boundary condition can be applied from Eq. (2.1.2k). Solving the Eq. (2.1.2i) under this boundary condition, and considering a rectangular box for the cavity aligned with the coordinate axes (x,y,z), yields [20]:

$$p_1(x, y, z) = p_a \cos(k_x x) \cos(k_y y) \cos(k_z z), \tag{2.1.3a}$$

$$\text{with} \quad k_j = n_j \frac{\pi}{L_j}, \quad n_j = 0, 1, 2, 3, \dots$$

These mode shapes, obtained in the equation above Eq. (2.1.3a), represent standing waves within the cavity, and determine the locations of the pressure nodes and antinodes within the microchannel.

2.1.4 Acoustic Impedance

Acoustic impedance describes the resistance to the propagation of sound waves within a material and indicates how effectively and in which manner (absorption, reflection, or transmission) an acoustic wave is transferred between two materials. The acoustic impedance is defined as:

$$Z = \rho c, \tag{2.1.4a}$$

where ρ is the density, c is the speed of sound [22], [23]. The transmission coefficient T and the reflection coefficient R can be then expressed by the acoustic impedances Z_1 and Z_2 of two materials as [24]:

$$T = \frac{4Z_1 Z_2}{(Z_1 + Z_2)^2} \tag{2.1.4b}$$

$$R = \left(\frac{Z_2 - Z_1}{Z_2 + Z_1} \right)^2 . \tag{2.1.4c}$$

The understanding of acoustic impedances at the interfaces of the experimental setup is enabling us to predict the efficiency of energy transfer from IDT to microchannel.

2.1.5 Acoustic Radiation Force

The acoustic radiation force (ARF), in general, consists of two components: the acoustic gradient forces *(primary acoustic radiation forces)* and the scattering forces *(secondary acoustic radiation forces)*, where the gradient forces are proportional to r^3 (r is the radius of the particle) and the scattering forces are proportional to r^6. This relationship makes the scattering forces negligible for small particles compared to the gradient pressure forces [4], which applies to the particles used in this thesis, as their radii are on the order of micrometers. Thus, only the primary ARF is discussed further.

Originally derived by Gorkov [21], the primary ARF on a compressible particle is described by the time-averaged gradient of the Gorkov potential,

$$F^{\text{rad}} = -\nabla U^{\text{rad}} = -\nabla \frac{4\pi}{3} r^3 \left[f_1 \frac{1}{2} \kappa_0 \langle p_{\text{in}}^2 \rangle - f_2 \frac{3}{4} \rho_0 \langle v_{\text{in}}^2 \rangle \right] \tag{2.1.5a}$$

$$f_1(\tilde{\kappa}) = 1 - \tilde{\kappa}, \quad \tilde{\kappa} = \frac{\kappa_p}{\kappa_0}, \tag{2.1.5b}$$

$$f_2(\tilde{\rho}) = \frac{2(\tilde{\rho} - 1)}{2\tilde{\rho} + 1}, \quad \tilde{\rho} = \frac{\rho_p}{\rho_0}. \tag{2.1.5c}$$

where U^{rad} is the acoustic radiation potential, r is the radius of the particles, f_1, f_2 are the coefficients of monopole and dipole scattering, respectively, and κ_0, ρ_0, κ_p, and ρ_p are the compressibility and density of the fluid and particles, respectively. $\langle p_{\text{in}} \rangle$ and $\langle v_{\text{in}} \rangle$ represent the averaged incoming pressure and velocity fields.

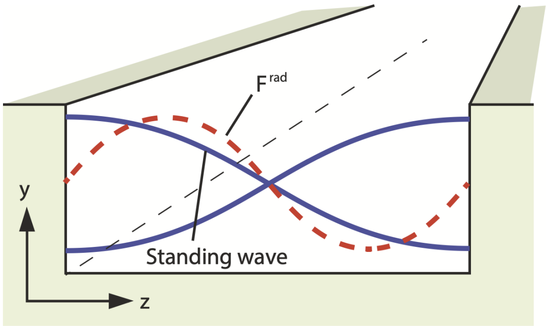

Figure 2.2: Schematic of 1D acoustic standing wave (blue solid line) and resulting acoustic force (red dashed line) [2]

.

For the 1D case with a standing wave of length $\lambda/2$ in a microfluidic channel (Fig. 2.2), the acoustic radiation force F^{rad} can be simplified to the following equation:

$$F_z^{\text{rad}} = -\partial_z U^{\text{rad}} = 4\pi\phi(\tilde{\kappa}, \tilde{\rho}) k r^3 E_{\text{ac}} \sin(2kz) \tag{2.1.5d}$$

$$E_{\text{ac}} = \frac{p_a^2}{4\rho_0 c_0^2} \tag{2.1.5e}$$

$$\phi(\tilde{\kappa}, \tilde{\rho}) = \frac{1}{3} \left[\frac{5\tilde{\rho} - 2}{2\tilde{\rho} + 1} - \tilde{\kappa} \right] \tag{2.1.5f}$$

Above, $\phi(\tilde{\kappa}, \tilde{\rho})$ is the acoustic contrast factor (ACF), k is the wave number $(2\pi/\lambda)$, z is the particle's position, E_{ac} is the density of acoustic energy, p_a is the pressure amplitude, ρ_0 is the density of the liquid and c_0 is the speed of sound in the liquid [2].

The ACF $\phi(\tilde{\kappa}, \tilde{\rho})$ determines if the particle moves toward the pressure node (for a positive ACF) or toward the pressure antinode (for a negative ACF) [4], as shown in Fig. 2.3. Particles that are denser and less compressible than the surrounding medium have a positive acoustic contrast factor, as is the case for polystyrene particles [25].

Conversely, particles with significantly lower density and higher compressibility than the surrounding liquid, have a negative contrast factor, as is the case for microbubbles [26].

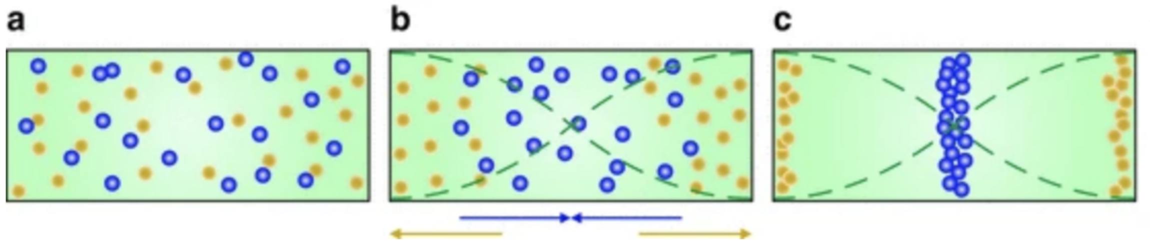

Figure 2.3: Illustration of particles with positive ACF (blue) and negative ACF (yellow), exposed to an acoustic standing wave field (green dashed lines), with the pressure node in the center and the antinodes at the walls [27].

2.1.6 Drag Force

In addition to the primary ARF, particles are also exposed to the Stokes drag force induced by acoustic streaming, Fig. 2.4, and/or background fluid flow in the microchannel.

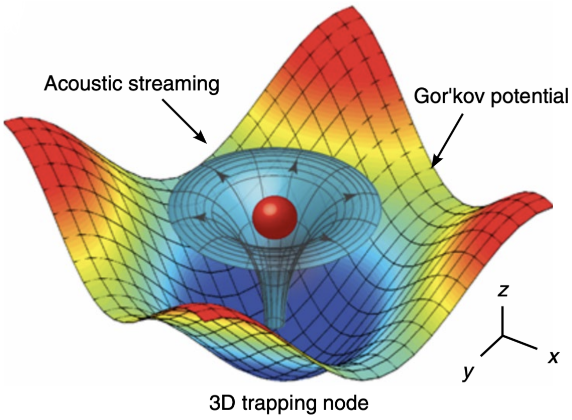

Figure 2.4: "Numerical simulation results show the mapping of the acoustic field around a single particle that demonstrates the operating principle for 3D manipulation with standing-wave tweezers [7]."

The Stokes drag force counteracts the primary ARF, and is given by:

$$\mathbf{F}_D = 6\pi\mu r(\mathbf{v}_{\text{str}} + \mathbf{v}_0 - \mathbf{v}_{\text{prt}}) \tag{2.1.6a}$$

Above, μ is the dynamic viscosity of the fluid, $\mathbf{v_{str}}$ is the streaming velocity, $\mathbf{v_0}$ is the background flow velocity, and $\mathbf{v_{prt}}$ is the particle velocity [2], [28].

When comparing Eq. (2.1.6a) with Eq. (2.1.5d), one can see that the drag force scales with r while the primary ARF scales with r^3. This difference in scaling behavior indicates that the primary ARF decreases much faster for smaller particles than the Stokes drag force. As a result, the drag force becomes the dominant force with decreasing radius, thereby disrupting particle confinement [29].

2.1.7 Surface Acoustic Waves

SAWs are generated using SAW devices, which generally consist of one or multiple IDTs, to be discussed in detail in the next section. The most common waves generated by SAW devices are Rayleigh waves, which propagate along the surface of the substrate, as shown in Fig. 2.5. Rayleigh waves have strong interactions with the liquid and the particles suspended within it, which makes them suitable for particle manipulation [15].

SAWs can be classified into traveling surface acoustic waves (TSAWs) and standing surface acoustic waves (SSAWs). TSAWs are generated by a single IDT, as illustrated in Fig. **??**, while SSAWs, on the other hand, are created by the superposition of two or more TSAWs interfering with each other [15]. This can be achieved by placing two IDTs opposite to each other, as shown in Fig. 2.5, and can also occur if the TSAW propagates through the liquid of a microfluidic chamber and is reflected at the water-glass/PDMS interface due to the significant acoustic impedance mismatch between water and glass/PDMS [30]. SSAWs create stable nodal positions which can be used for particle trapping, as indicated by red (antinode) and green (positive node) points in Fig. 2.5(b).

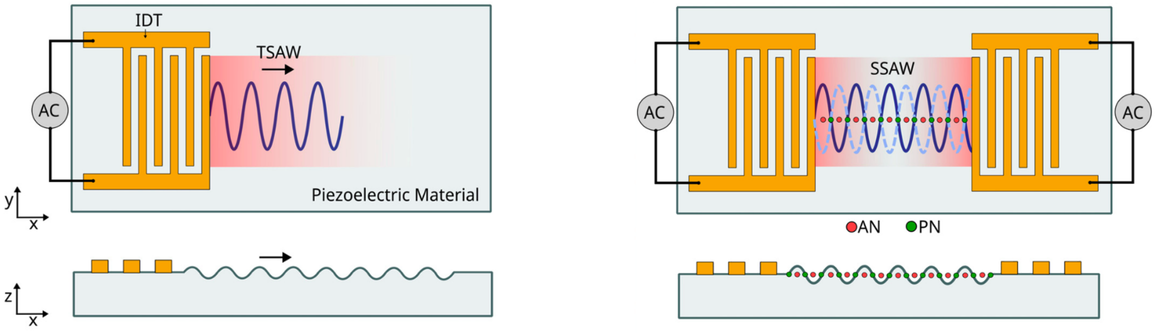

(a) (b)

Figure 2.5: Schematic illustrations SAW generation: (a) A single IDT producing a TSAW, and (b) two opposing IDT's generating a SSAW [15]

At the interface between a SAW device and a liquid-filled microfluidic chamber, the surface acoustic wave propagates into the fluid at the Rayleigh angle (θ_R), shown in Fig. 2.6 given by the following relationship:

$$\sin(\theta_R) = \frac{c_f}{c_s}, \tag{2.1.7a}$$

Above, c_f and c_s are the speed of sound in the fluid and the substrate, respectively [31].

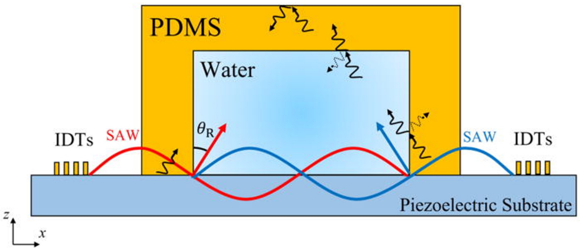

Figure 2.6: Schematic illustration in cross-sectional view of SAW propagation into microfluidic chamber [14].

In addition to fundamental Rayleigh waves, there are other types of SAWs, such as Sezawa waves, Lamb waves, shear horizontal SAWs and Love waves [15]. These wave types are not discussed further since they are not relevant for this thesis.

2.2 Interdigital Transducers

Interdigital transducers were first developed in 1965 by White and Volmer [32] and have since been used in various applications such as radar, telecommunications, and more recently, in high-precision ultrasonic manipulation of fluids [31]. As briefly mentioned in the introduction, IDTs are interlocking, "finger-like" electrodes. Typically, they are embedded in a piezoelectric substrate; the most common substrates are quartz, lithium niobate ($LiNbO_3$), or lithium tantalate ($LiTaO_3$) [15]. By applying an AC current to the piezoelectric substrate, they are able to generate mechanical oscillations that propagate as SAWs on the surface of the substrate.

In the following, the physical phenomenon of piezoelectrics, on which the IDTs are based, as well as different IDT designs are discussed further.

2.2.1 Piezoelectric Effect

The piezoelectric effect converts mechanical energy into electrical energy, whereas the reverse piezoelectric effect converts electrical energy into mechanical energy.

To understand this relationship further, we first look at a nonpiezoelectric material. For a nonpiezoelectric material, a mechanical displacement u induces a stress $T = c\partial_z u$, and an electrical displacement D generates an electric field $E = \frac{D}{\varepsilon}$, with ε being the electric permittivity of the material. Assuming an insulator and electroneutral material (as is the case for most piezoelectric materials), the relation between electric current and electric displacement is:

$$\frac{\partial D}{\partial t} = \frac{I(t)}{A} \tag{2.2.1a}$$

Considering now a piezoelectric material, where the electrical and mechanical fields are entangled, the stress is given as:

$$T = c^D \frac{\partial u}{\partial z} - \left(\frac{e}{\varepsilon}\right) D, \tag{2.2.1b}$$

where e is the piezoelectric coupling coefficient, c^D is the stiffness at constant electric displacement ($c^D = c^E + \frac{e^2}{\varepsilon}$), with c^E being the stiffness at constant electric field.

Taking the time derivative of the stress equation and substituting in the expression for the electric displacement of Eq. (2.2.1a) yields:

$$\frac{\partial T}{\partial t} = c^D \frac{\partial v}{\partial z} - \frac{e}{A\varepsilon} I(t). \tag{2.2.1c}$$

In the above equation, stress, mechanical vibration, and electric current are now coupled. Using Newton's law $\rho \partial_t^2 v = -\partial_z T$, the equation for a plane longitudinal electroacoustic wave propagating through a piezoelectric material can be found as [31], [33]:

$$\rho \frac{\partial^2 v}{\partial t^2} = c^D \frac{\partial^2 v}{\partial z^2}. \tag{2.2.1d}$$

The piezoelectricity of materials arises from their non-centrosymmetric crystal structure, which enables displacements between anions and cations. Due to these properties, a charge can be generated by stress-induced displacement of the crystal structure [34].

In simple terms, the crystal structure of the unit cell can be visualized as in Fig. 2.7, where the atom, indicated with a "B", is displaced, shifting the center of negative and positive charges so that they no longer coincide, resulting in an electric dipole [35].

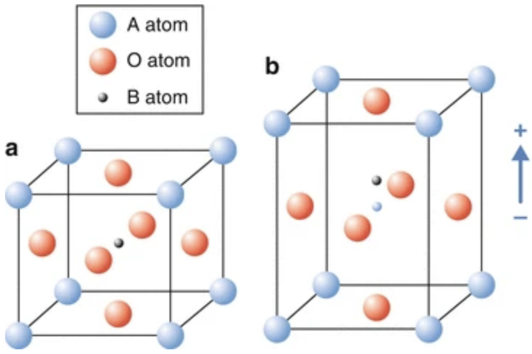

Figure 2.7: Schematic illustration of a piezoelecric unit cell crystal structure [35].

As elaborated in Chapter 1, this also works in reverse: applying a voltage to the piezoelectric material leads to a deformation of the crystal structure.

2.2.2 IDT Design

There are many ways to design the geometry, spacing, and dimensions of IDTs. The specific configuration is highly application-dependent. The design variations can be optimized for various use cases, such as mixing, concentrating/trapping, patterning, or sorting. These differences may be in shape (straight or curved), electrode thickness, and spacing [15].

During this project, straight IDTs (Fig. 2.8) were employed for patterning, as the superposition of their acoustic waves generates a checkered interference pattern (see in Fig. A.3 in the Appendix). However, the primary focus of this project was particle trapping and manipulation. For this purpose, curved IDTs, as shown in Fig. 2.8, were used. These transducers create a single pressure node at the focal point through constructive interference of the SAWs. Furthermore, dividing them into four sections allows the actuation of only one pair of opposing IDTs, which is essential for deforming particle clusters in the central pressure node. Both designs feature regularly alternating electrodes.

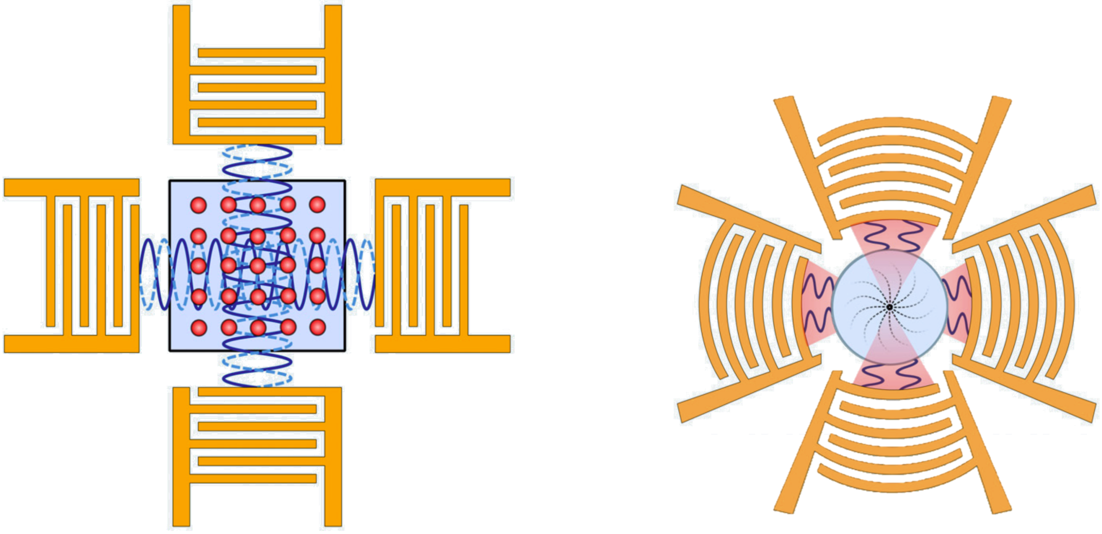

(a) (b)

Figure 2.8: Illustration of IDT designs: (a) Straight IDT design and (b) Curved/focused IDT design [15]

The wavelength (λ_R) of the SAW generated by the IDT depends on the periodicity of the IDT-finger pairs. The distance between two fingers is equal to $\lambda_R/4$, as illustrated in Fig. 2.9.

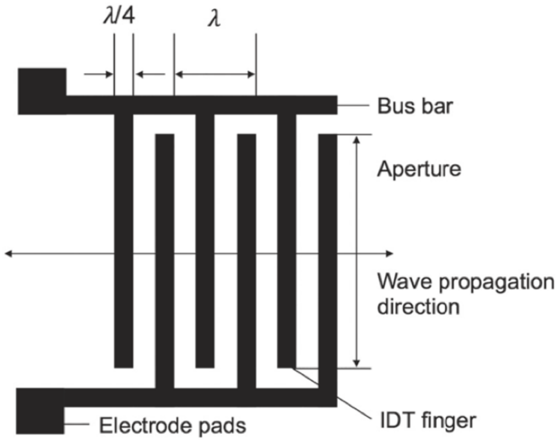

Figure 2.9: Schematic illustration of IDT components [31]

The phase velocity of the SAW (v) is determined by the material properties of the substrate, including its elastic constant and density. Using this velocity, one can calculate the theoretical resonance frequency (f), shown in Eq. 2.2.2a, at which the IDT exhibits peak response, which means that the IDT achieves maximum energy conversion into mechanical vibrations.

The expression for the resonance frequency is given as:

$$f = \frac{v}{\lambda_R} \tag{2.2.2a}$$

Another essential parameter in IDT design is the power radiated by the IDT, which is given by:

$$\langle P \rangle = \frac{1}{2} G_a |U|^2, \tag{2.2.2b}$$

where G_a is the conductance and U the applied voltage. The conductance depends on the number of pairs of electrode fingers and the static capacitance of the IDT [31].

2.3 Zebrafish Model

Zebrafish have become a widely used vertebrate model for cardiovascular research over the last few decades. The advantages of the zebrafish model include practical genetic manipulations, as well as the transparent nature of the zebrafish during embryonic stages. This allows for direct visualization of the vasculature under the microscope [36].

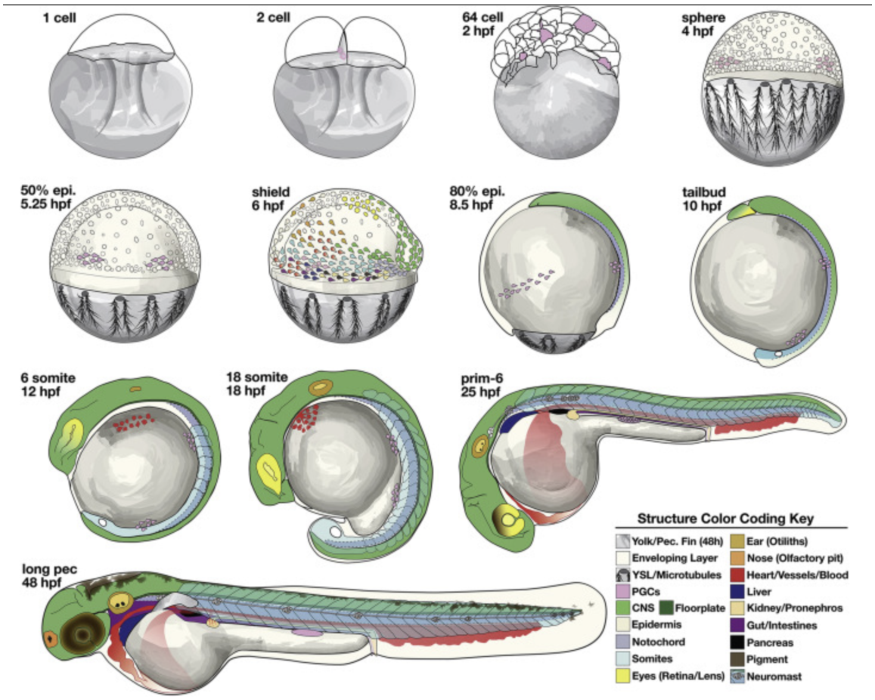

Figure 2.10: Illustrative overview of the embryonic development of zebrafish [37]

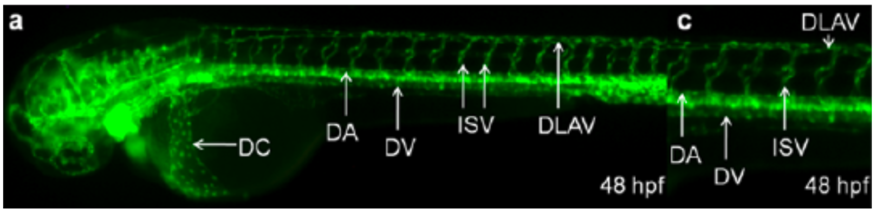

Figure 2.11: Vasculature of a 48-hpf zebrafish embryo. DC: Duct of Curvier; DA: Dorsal aorta; DLAV: Dorsal longitudinal anastomotic vessels; DV: Dorsal vein; ISV: Inter-segmental vessel; SIV: sub-intestinal vessels [38]

The embryonic stages are classified in hours post fertilization (hpf) or days post fertilization (dpf), as shown in Fig. 2.10. The velocity of blood flow varies depending on the age of the zebrafish and peaks at 3-dpf, as shown in Fig. 2.12. The dorsal aorta (diameter of approx. 36 μm [39]), depicted in Fig 2.11, is the main vessel exhibiting the highest flow velocities. Knowledge of blood flow velocity is essential for particle trapping, as faster blood flow introduces a stronger drag force on particles.

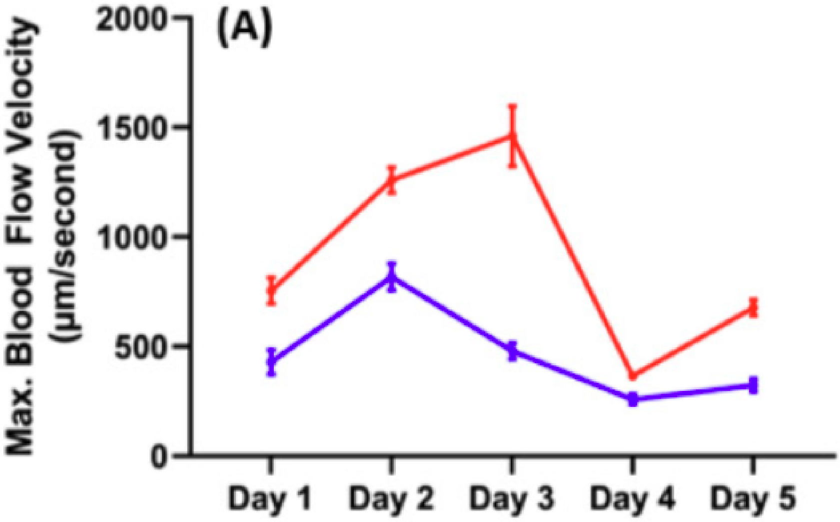

Figure 2.12: Maximum blood flow velocity of zebrafish embryos aged 1-5 dpf in dorsal aorta (red) and posterior cardinal vein (blue) [40].

Chapter 3

Materials and Methods

This chapter outlines the materials, fabrication processes, and experimental setups used for this project. It describes the creation and characterization of devices, the preparation of microfluidic and biological systems, and the procedures used in both *in vitro* and *in vivo* experiments.

3.1 Fabrication

In the following, the fabrication procedures of the IDTs used in the *in vitro* characterization and the *in vivo* experiments, as well as the microfluidic chambers employed for the *in vitro* trials, are described.

3.1.1 IDT Fabrication

The IDT design was first determined using CAD software. The fabrication steps were conducted in the clean room of the ARSL laboratory. There, a wafer made of 128 ° Y cut X-propagating lithium niobate (LiNbO3), which serves as a piezoelectric substrate, was selected because it generates SAWs with high efficiency [41]. The wafer was then subjected to a standard UV photolithography process, including spin coating with a photoresist, baking, photomask alignment of the inverse IDT design, UV light exposure, and gold vapor deposition [42].

After these fabrication steps were completed in the clean room, the electrodes of the IDT devices were connected with wires by soldering. This procedure is very sensitive, as the heat of the soldering iron induces thermal stress, which can easily cause the piezoelectric substrate to crack. To ensure reliability and quality in these steps, they were carried out by the thesis supervisor, Hemin Pan.

The FIDTs fabricated and used primarily for this project are depicted in Fig. 3.1. These widths were chosen to achieve the desired operational frequencies.

	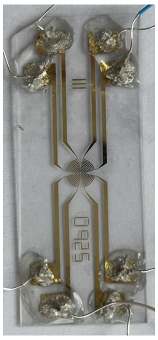	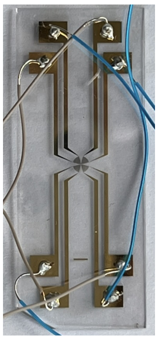
electrode width [μm]	50	25
resonance frequency [MHz]	39.2 & 59.3	42.2 - 49.5

Table 3.1: FIDTs used primarily in this project

3.1.2 Microfluidic Chamber Fabrication

Following, the consecutive steps of microfluidic chamber fabrication are described in detail:

1. Mold Fabrication

The first step in the chamber fabrication process was to create a mold. This involved preparing a silicon wafer patterned with the desired chamber geometries. The chamber geometries were designed in advance using CAD software. The wafer was patterned using a photolithography machine in the clean room at ARSL. This step was performed by the thesis' supervisor, Hemin pan.

2. Silanization of Wafers

The next steps of the fabrication process of the microfluidic chambers were performed in the wet lab at ARSL. Here, the patterned wafers were treated to make their surface hydrophobic by silanization. This was achieved by placing them into a vacuum chamber together with some droplets of (3-Aminopropyl)triethoxysilane, as shown in Fig. 3.1. The vacuum chamber was then decompressed to about 10 mbar. In this environment, the silane evaporates and reacts with the wafer's surface to make it hydrophobic. After an hour of silanization, the wafers were removed from the vacuum chamber.

3. PDMS Casting and Curing

In a next step, a 10: 1 ratio of the PDMS base (SYGARD 184 silicon elastomer) to the curing agent was mixed, enabling the PDMS to harden in the oven later on. This mixture was first degassed in the vacuum chamber and then poured over the silanized mold, Fig. 3.2. The wafer with the PDMS mixture on top was degassed once more to ensure complete removal of air bubbles. After that, the wafers coated with the PDMS mixture were placed in the oven at 80°C to cure.

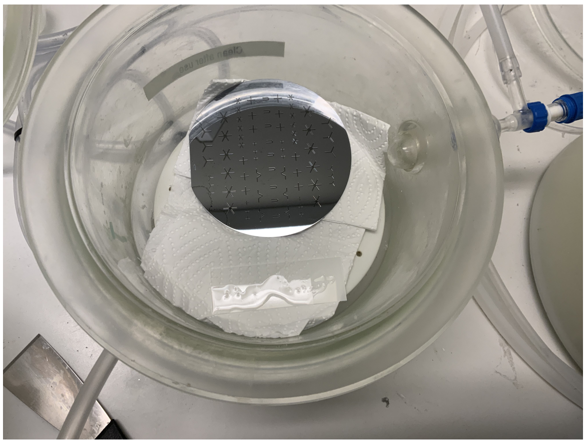

Figure 3.1: A 4-inch silicon wafer next to a glass slide with droplets of silane on it, placed in a vacuum chmaber.

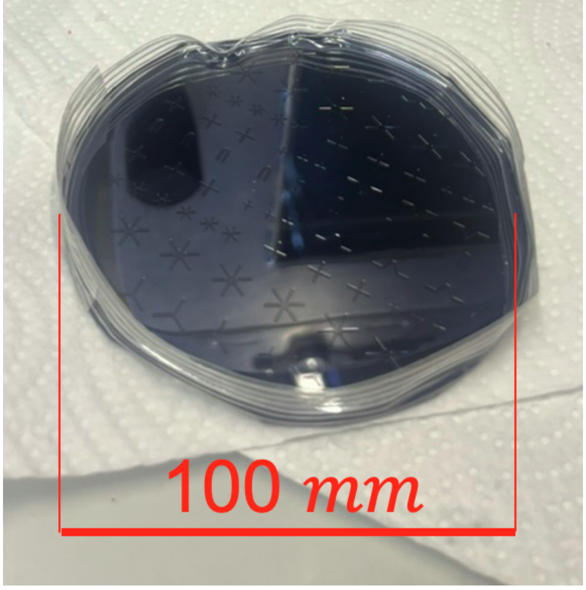

Figure 3.2: 4-inch silicon wafer coated with the PDMS mixture

4. Chamber Extraction and Bonding

After curing, the PDMS was peeled off the mold and the individual chambers were cut out using a razor blade, as shown in Fig. 3.3. These single PDMS chambers were bonded to a glass slide, to form a complete microfluidic chip. To do so, the chambers, immersed in IPA, first had to be cleaned using an ultrasonic cleaner. After cleaning, the surfaces of the PDMS and the glass slides were treated with a plasma cleaner (PiezoBrush PZ3, Relyon plasma), which activates the surfaces and enables enhanced adhesion between the glass slide and PDMS chamber. Once treated, the PDMS chambers were aligned and bonded to the glass slides. Finally, the prepared chips with the PDMS chambers were placed in the oven again for an hour at 80 ° C to ensure proper bonding.

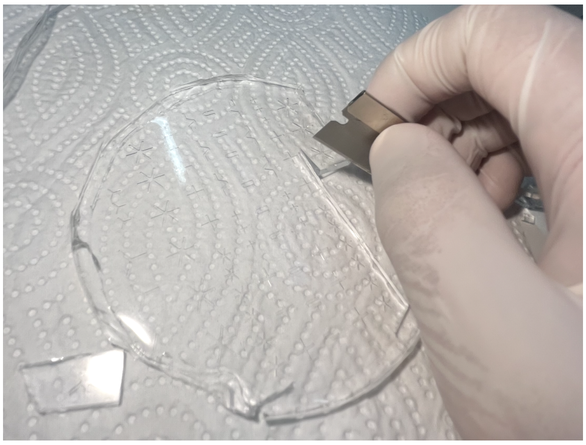

Figure 3.3: Cutting free the PDMS chambers with razor a blade

3.2 Experimental Setup

The *in vitro* experiments were carried out in the acoustic robotics systems laboratory (ARSL), while the *in vivo* trials were carried out in the laboratory of the Institute of Molecular Life Sciences at the Irchel campus of the University of Zürich.

3.2.1 *In Vitro* Experimental Setup

In the *in vitro* experiments for IDT characterization and blood vessel simulation, the following setup was utilized.

The AC signal for IDT actuation (**E**) was generated using a function generator (**A**: 0-60MHz, 0.1-5.0 V_{pp}, Tektronix AFG1062, Tektronic, Inc., US)) and a high-frequency amplifier (**B**: 25A250ions a AM6, Amplifier Research). For observations, a camera (**C**: THORLABS, fps = 8.8) connected to a microscope (**D**: Zeiss Axiovert 200M) was used, as shown in Fig. 3.4 & Fig. 3.5. The microfluidic chamber, which contains the particle solution, as shown schematically in Fig. 3.6, was placed on top of the IDT, with a droplet of a glycerol-based gel serving as an intermediary layer to ensure effective acoustic coupling. The solutions for the polystyrene (PS) particles and microbubbles were made using phosphate buffered saline PBS, while those containing yeast cells were made using DI water. The particles used in the *in vitro* experiments are shown in Table 3.2 below. This setup enables precise control over the acoustic field and direct visualization of particle behavior.

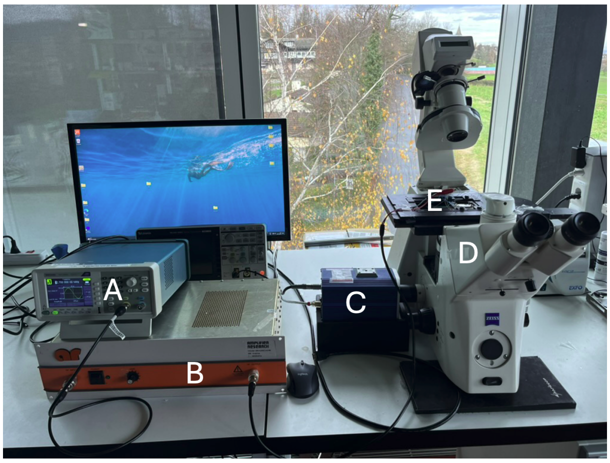

Figure 3.4: Experimental setup at ARSL

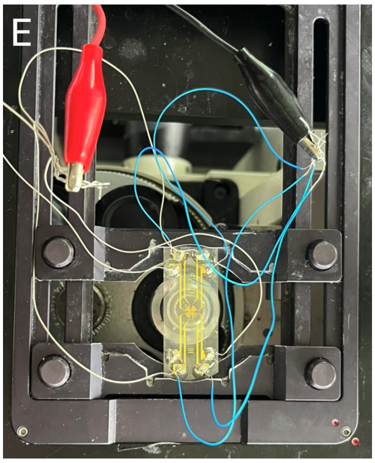

Figure 3.5: IDT mounted on a microscope and connected to the amplifier

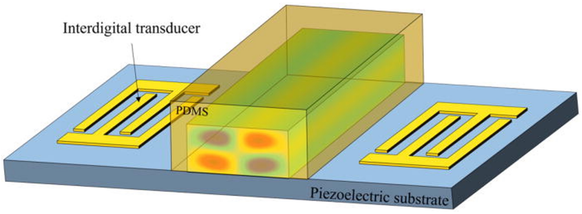

Figure 3.6: Schematic illustration of PDMS channel filled with aqueous solution placed on top of a SAW device [14].

Particle Type	**Diameter [μm]**	**ACF**
Polystyrene particles	1.0	Positive
Polystyrene particles	2.6	Positive
Microbubbles (USsphere Tracer FD-Red)	1.1 – 1.4	Negative
Yeast cells	5.0 – 10.0	Positive

Table 3.2: Particles used in *in vitro* experiments [43], [44].

3.2.2 *In Vivo* Experimental Setup

The *in vivo* experiments were performed in the Institute of Molecular Life Sciences on the Irchel Campus of the University of Zürich. The experiments were carried out using a fluorescent microscope (Leica M205 FCA, fps = 35.71), as shown in Fig. 3.7.

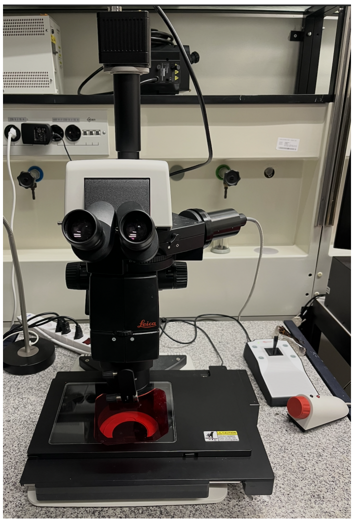

Figure 3.7: Fluorescent microscope from Leica used for the *in vivo* experiments.

For the experiments, 48-hpf zebrafish embryos were used. They were prepared and injected with fluorescent particles and microbubbles by Dr. Zan. The use of fluorescent particles enable for better visualization of the particles' motion in the zebrafish's vasculature. To prevent zebrafish embryos from moving during the observations, they were first embedded in agarose gel. Subsequently, the glass slide with the embedded zebrafish embryo was placed under the fluorescent microscope on top of the FIDT, with a droplet of coupling gel serving as an intermediary layer. For IDT actuation, the same setup (function generator and amplifier) used in the *in vitro* experiments was employed. In Fig. 3.8 the zebrafish mounted on top of the FIDT is shown; the green area corresponds to the yolk of the zebrafish, where the green fluorescent particles were injected.

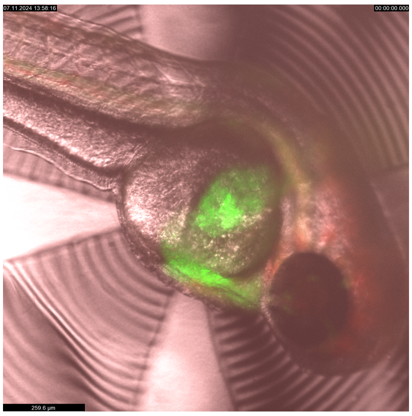

Figure 3.8: Zebrafish placed on top of the FIDT with green fluorescent particles injected.

3.3 Method for IDT characterization

To successfully capture and manipulate particles in a single pressure node within the zebrafish's vessel, focused SAW devices were employed. To ensure reliable results for the *in vivo* experiments, it was necessary to determine the resonance frequency of the focused IDT and study the behavior of particles of various diameters under the influence of SAW waves. The behavior was further examined under static conditions (zero flow velocity) and in the presence of controlled fluid flow, simulating the environment of a zebrafish's blood vessel.

3.3.1 Identification of Resonance Frequency

To identify the IDT's resonance frequency, the IDT was prepared as discussed in Chapter 3.2.1, under static conditions (zero flow velocity). The amplitude in the function generator was set to 1.0 V_{pp}, which was amplified with a gain of approximately 15x by the amplifier. By sweeping from low to high frequencies in the MHz range, the fundamental resonance frequency and its higher harmonics were identified. These frequencies were determined by observing the behavior of the particles and noting the frequencies that produced the strongest particle responses. These experiments were repeated several times with different types of particles, as listed in Table 3.2.

3.3.2 Testing Resonance Frequency under Controlled Fluid Flow

To more accurately simulate the conditions of the *in vivo* experiments more accurately, the fluid in the microfluidic channel was set in motion. This was achieved using the microfluidic channel shown in Fig. 3.9, which was filled with the particle solution, and placing a droplet of liquid on top of one opening. Capillary forces put the fluid in motion [45]. Once the fluid was in motion, the previously identified resonance frequencies were applied using the function generator, and the particles' behavior under these conditions was studied.

To test robustness of particle manipulation under non-optimal conditions, the fluid channel was deliberately misaligned with the IDT's focal point. Subsequently, the ability to manipulate particles under these conditions was evaluated.

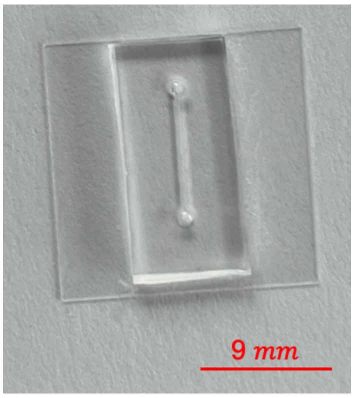

Figure 3.9: Microfluidic channel used for testing particle behavior under controlled fluid flow conditions

3.4 Measuring Velocities in Microfluidic Channel

To measure the velocity of particles or particle clusters, an image processing software (ImageJ) was utilized. A calibration step first determined the relationship between image pixels and the actual physical dimensions in micrometers. By tracking particle displacement and using the known microscope frame rate, the elapsed time over several frames was derived, enabling velocity measurement.

The following describes velocity calculations for the experimental setup with the offset fluid channel, Fig. 4.5. Velocity measurements in other experiments were performed analogously.

The known width of a single "electrode finger" ($50\ \mu m$) was compared to the number of pixels that span this width in the image. To reduce measurement inaccuracies, multiple measurements were performed, as shown in Fig. 3.10. The mean width ($w_{mean} = 77.925px$) was then calculated. The micrometer-to-pixel ratio ($\alpha_{\mu\text{m/px}}$) was calculated using the following relation:

$$\alpha_{\mu\text{m/px}} = \frac{50\mu m}{77.925px} = 0.6416\frac{\mu m}{px} \tag{3.3a}$$

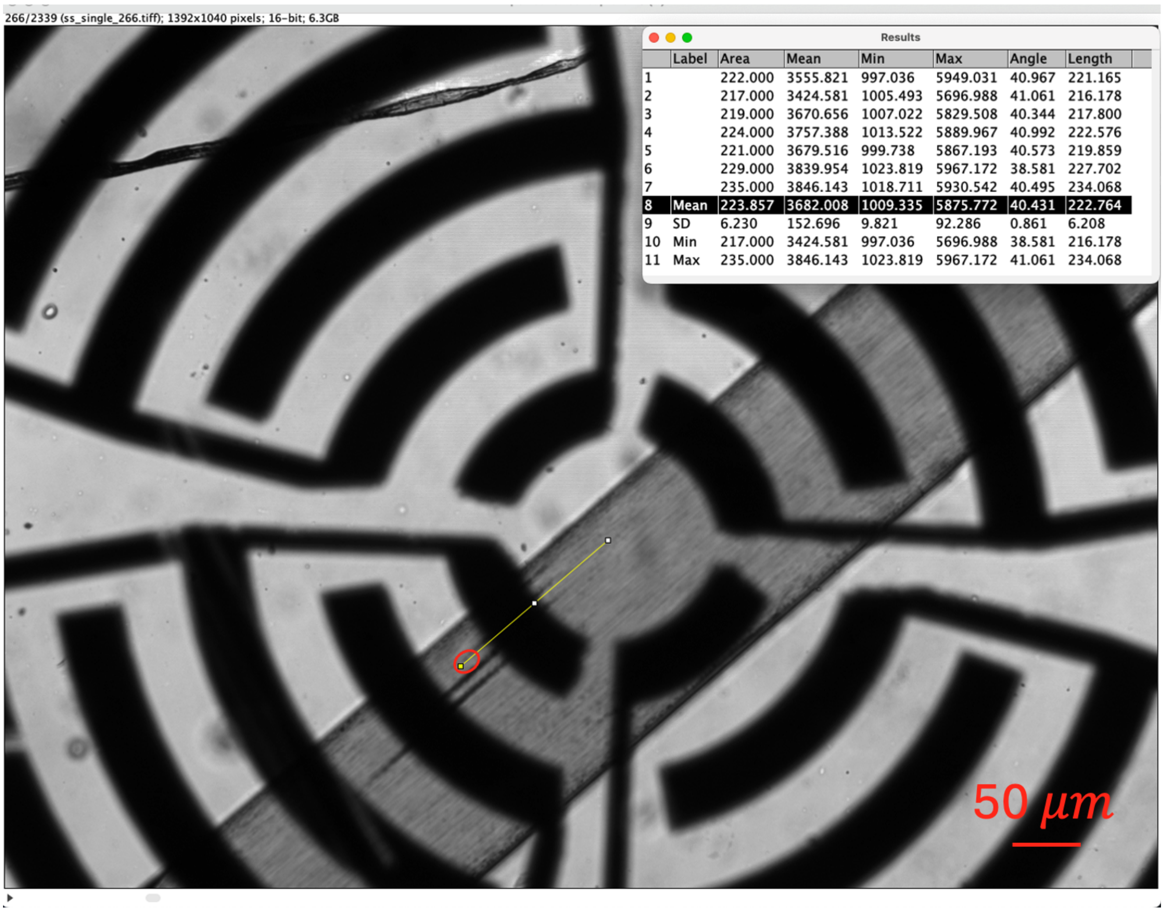
266/2339 (ss_single_266.tiff); 1392x1040 pixels; 16-bit; 6.3GB

Results

	Label	Area	Mean	Min	Max	Angle	Length
1		222.000	3555.821	997.036	5949.031	40.967	221.165
2		217.000	3424.581	1005.493	5696.988	41.061	216.178
3		219.000	3670.656	1007.022	5829.508	40.344	217.800
4		224.000	3757.388	1013.522	5889.967	40.992	222.576
5		221.000	3679.516	999.738	5867.193	40.573	219.859
6		229.000	3839.954	1023.819	5967.172	38.581	227.702
7		235.000	3846.143	1018.711	5930.542	40.495	234.068
8	Mean	223.857	3682.008	1009.335	5875.772	40.431	222.764
9	SD	6.230	152.696	9.821	92.286	0.861	6.208
10	Min	217.000	3424.581	997.036	5696.988	38.581	216.178
11	Max	235.000	3846.143	1023.819	5967.172	41.061	234.068

Figure 3.10: Measurement of a single electrode's width using ImageJ with the line tool (yellow). The particle cluster, highlighted in red, was tracked for velocity measurements.

The displacement of the particle cluster from the start to the end position was measured several times, and the mean displacement ($d_{mean} = 222.764px$) was calculated. Using Eq. 3.3a, the physical distance in micrometers was determined as:

$$d_{mean} = 142.935\mu m \tag{3.3b}$$

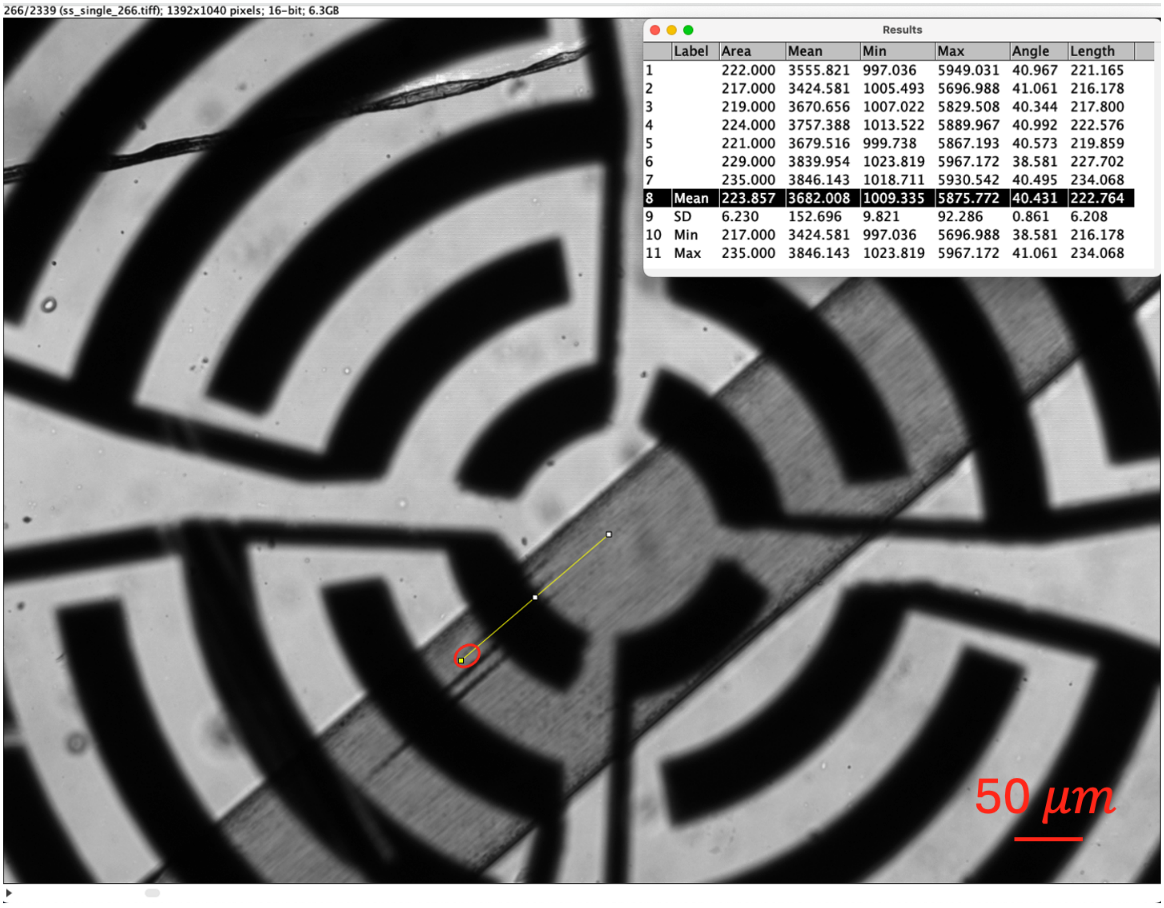

	Label	Area	Mean	Min	Max	Angle	Length
1		222.000	3555.821	997.036	5949.031	40.967	221.165
2		217.000	3424.581	1005.493	5696.988	41.061	216.178
3		219.000	3670.656	1007.022	5829.508	40.344	217.800
4		224.000	3757.388	1013.522	5889.967	40.992	222.576
5		221.000	3679.516	999.738	5867.193	40.573	219.859
6		229.000	3839.954	1023.819	5967.172	38.581	227.702
7		235.000	3846.143	1018.711	5930.542	40.495	234.068
8	Mean	223.857	3682.008	1009.335	5875.772	40.431	222.764
9	SD	6.230	152.696	9.821	92.286	0.861	6.208
10	Min	217.000	3424.581	997.036	5696.988	38.581	216.178
11	Max	235.000	3846.143	1023.819	5967.172	41.061	234.068

Figure 3.11: Measurement of the distance of the particle cluster's trajectory using ImageJ's line tool (yellow). The red circle highlights the cluster's end position.

The number of frames during the observation period ($\#frames = 5$) was counted. With the known frame rate ($fps = 8.8$), the elapsed time t in seconds was calculated:

$$t = \frac{\#frames}{fps} = 0.5682s, \tag{3.3c}$$

Finally, the particle velocity (v_{part}) was calculated as:

$$v_{part} = \frac{d_{mean}}{t} = 251.57\frac{\mu m}{s} \tag{3.3d}$$

3.5 *In Vivo* Manipulation of Particles in Zebrafish Embryos

The particle manipulation experiments in zebrafish embryos were conducted under the experimental setup described in Chapter 3.2.2. Zebrafish embryos (approximately 48 hpf) were injected with a praticle solution, by Dr.Zang. The experiments were carried out with three types of particles, as listed in Table 3.3.

Particle type	Product	Diameter $[\mu m]$	Density $[\frac{g}{cm^3}]$	*Excitation $[nm]$
Fluorescent particle (PS)	Novus Biologicals Jade Green	1.0	**1.05	**700
Fluorescent particle (PS)	Spherotech Nile Red	1.0	**1.05	515 - 530
Fluorescent microbubble	USphere Tracer FD-Green	1.1 - 1.4	**1.025	484
Fluorescent microbubble	USphere Tracer FD-Red	1.1 - 1.4	**1.025	549

Table 3.3: Table of all the particles used in the zebrafish experiments. *The Excitation column refers to the excitation wavelength of the light used to excite the fluorescent dye in the particle/bubble. The data highlighted with (**) is not the exact data for the product, but approximate values found in other sources [46], [47] [48].

Chapter 4

Results

The primary aim of this project was to manipulate particles within zebrafish embryos. To achieve this goal, preliminary experiments were conducted to characterize the IDTs intended for the zebrafish trials. In addition, simulations of blood vessels with similar dimensions were performed using PDMS channels and controlled fluid flow.

Following these preparatory steps, the *in vivo* experiments on the zebrafish embryos were conducted.

In the top left corner of the figures provided in this chapter, a schematic illustration of the IDTs is indicating, whether a section of the IDT is actuated (colored blue) or deactivated (colored white).

4.1 Characterization of IDTs

The following section describes the characterization of the FIDT with an individual electrode width of 50 μm. The voltage amplitude was set in the range of $0.7V_{pp}$ to $1.3V_{pp}$. The characterization results for the FIDT with an individual electrode width of 25 μm are provided in the Appendix, shown in Fig. A.1 & Fig. A.2, as they yielded noteworthy observations. However, under conditions that involve rapid fluid flow, the FIDT with a 50 μm electrode width demonstrated superior performance. This enhanced effectiveness is likely attributed to its ability to generate a stronger ARF to counteract the strong drag force under fluid flow conditions, compared to the smaller electrode design.

At a frequency of 39.2 MHz, a distinct single-point aggregation of particles was observed at the center of the pressure node, as shown in Fig. 4.1. This frequency corresponds to a harmonic of the vibrational resonance modes exhibited by the tested FIDT, as it was the first frequency that showed a strong particle response. In this first experiment, the fluid in which the PS particles are suspended remained static (zero velocity).

Figure 4.1: FIDT manipulating/capturing PS particles at a resonance frequency of 39.2 MHz, in a channel with a width of 300 μm and a height of 240 μm

By shifting back and forth across the resonance frequency, deformations of the particle cluster were induced both along the channel axis and perpendicular to its orientation, as shown in Fig. 4.2.

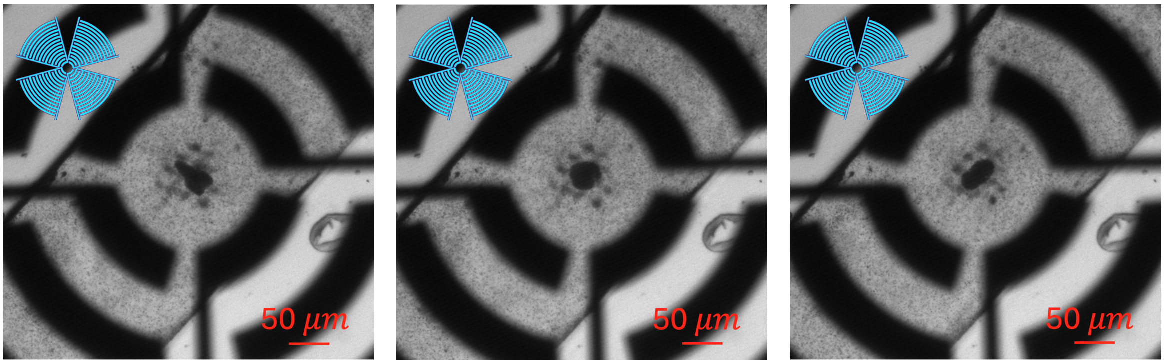

(a) Deformation perpendicular to the channel orientation ($t = 0s$)

(b) No deformation ($t = 1.59s$)

(c) Deformation along the channel orientation ($t = 10.34s$)

Figure 4.2: Time-sequential visualization of deformation of a single dot particle cluster under acoustic excitation at 39.2 MHz.

After continuously increasing the frequency even higher, an additional higher harmonic was found at 59.3 MHz. At this frequency, significantly stronger acoustic streaming was observed, compared to 39.2 MHz. This is illustrated in Fig. 4.3, where the red ellipses denote the regions in which streaming was occurring, and the red arrows represent the direction of the streaming motion. The streaming motion was observed to transition very clearly from a single nodal point, when all four FIDT sections were actuated, Fig. 4.3(a), to a single nodal line when only two opposing FIDT sections were actuated, Fig. 4.3(b) & Fig. 4.3(c). Additionally, a single single-point aggregation could not be formed, as was possible at 39.2 MHz. Instead, a higher harmonic pattern with multiple pressure nodes forming a checkered pattern at the focal point of the FIDT, as depicted in Fig. 4.3b.

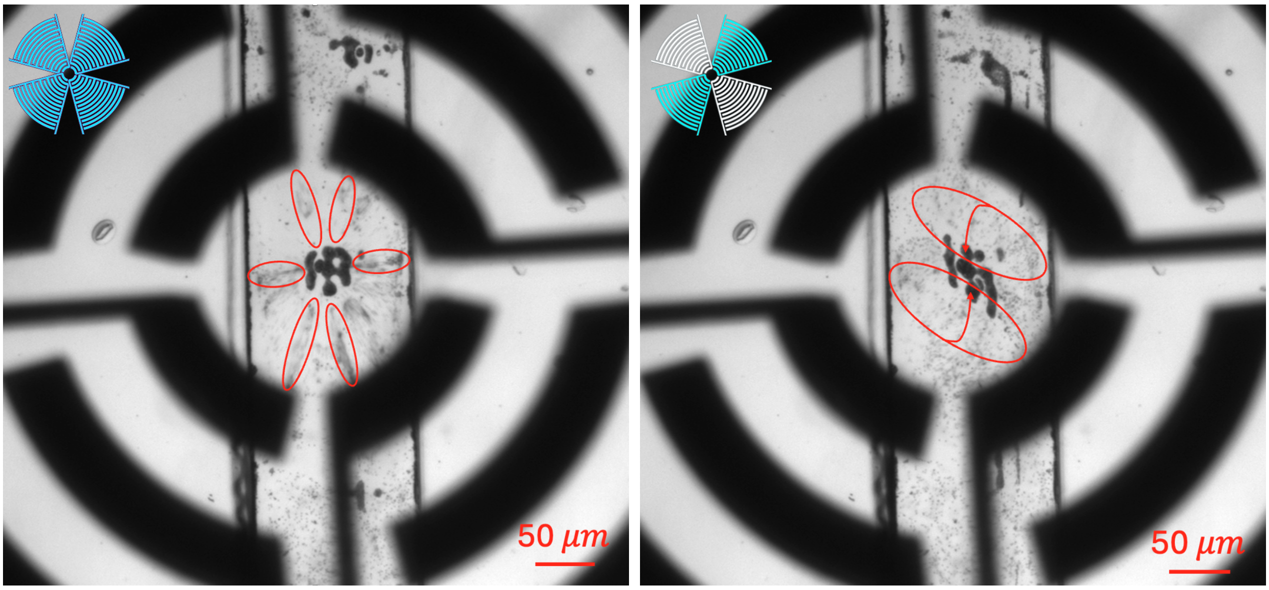

(a) Only one pair of opposing FIDT sections actuated, highlighted in red.

(b) All four FIDT sections actuated, highlighted in red.

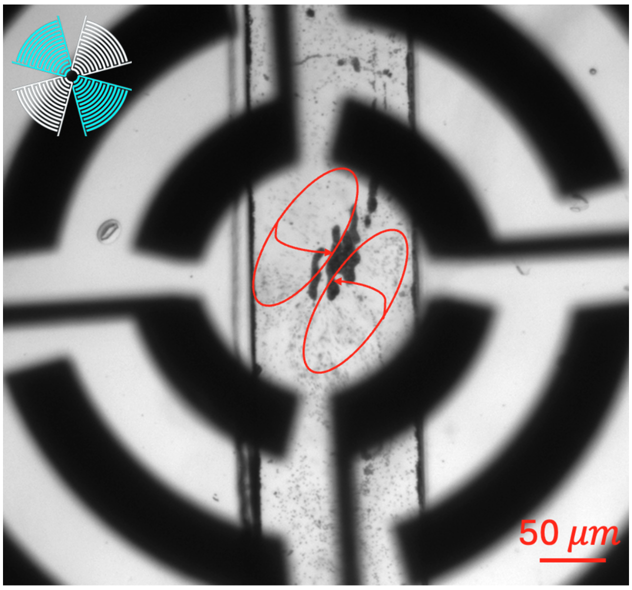

(c) Only one pair of opposing FIDT sections actuated, highlighted in red.

Figure 4.3: Deformation of patterned particle cluster at 59.3 MHz

4.2 *In Vitro* Simulation of Blood Flow

The PS particles could be captured successfully at the focal point of the FIDT, even under controlled fluid flow conditions. However, this was only achieved at the higher harmonic frequency of 59.3 MHz, Fig. 4.4. Despite the successful capturing, a single dot of accumulated particles was not observed. Instead, a pattern of straight lines, parallel to the channel, was formed in the focal point of the SAW device. This pattern was located at a different height within the channel, farther from the FIDT, compared to the single line of accumulated particles indicated by the red arrow in the figure.

The velocity of the captured particles after deactivation of the FIDT was calculated to be 400.16 $\mu m/s$, which is significantly lower than the maximum flow velocity measured for 48-hpf zebrafish embryos of approximately 1200 $\mu m/s$, as reported in literature [40].

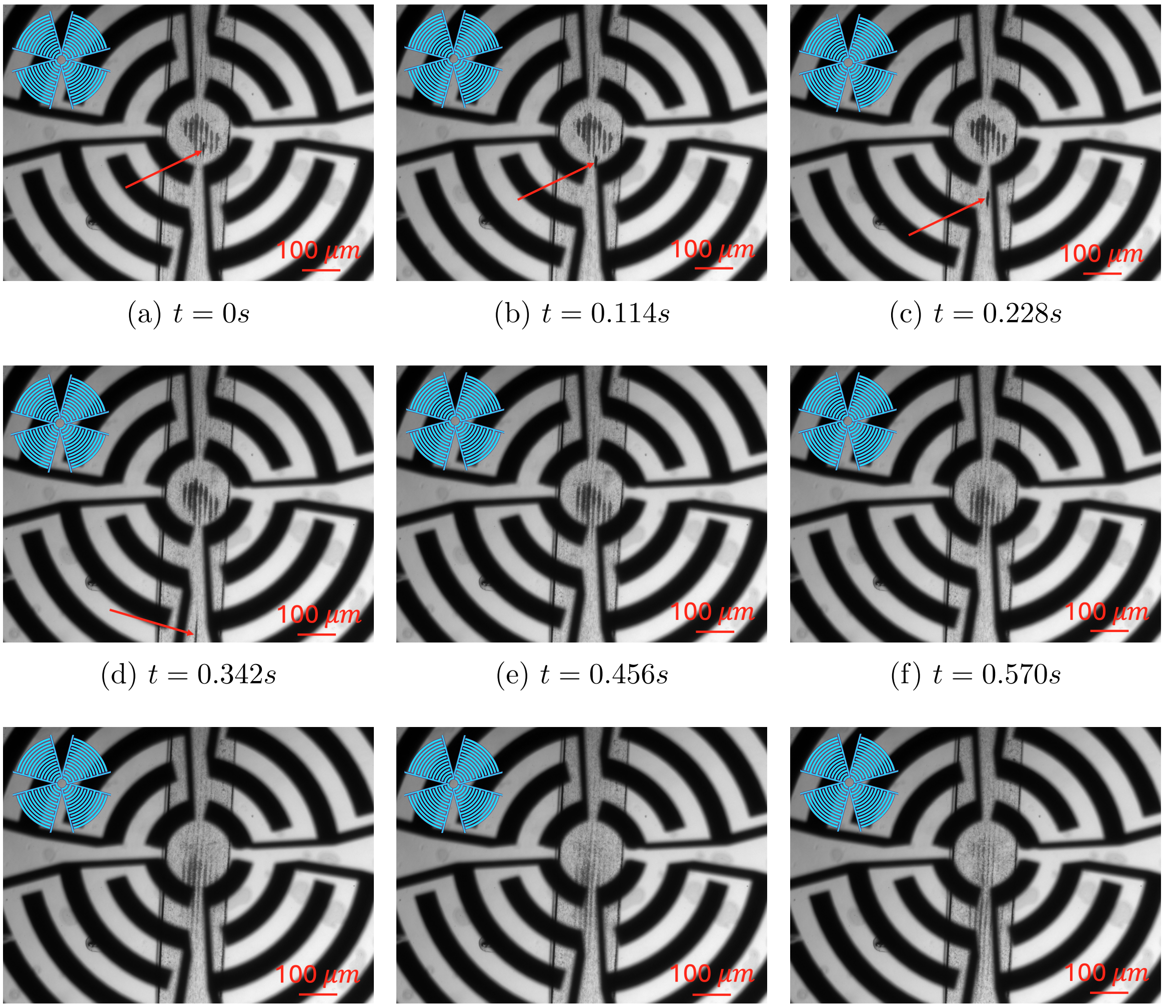

(a) $t = 0s$ (b) $t = 0.114s$ (c) $t = 0.228s$

(d) $t = 0.342s$ (e) $t = 0.456s$ (f) $t = 0.570s$

(g) $t = 0.684s$ (h) $t = 0.798s$ (i) $t = 0.912s$

Figure 4.4: Time-sequential visualization of polystyrene particles, initially captured, being displaced and carried away by the fluid flow, upon deactivation of the FIDT. The width of the channel was 300 μm and the height was 240μm.

Even when adjusting the setup, such that the fluid channel was offset relative to the focal point of the FIDT, it was still possible to capture PS particles during controlled fluid flow. However, as in the previous configuration, this was only achieved at a frequency of 59.3 MHz. Similarly to the previous experiment (see Fig. 4.5, the observed pattern consisted of straight lines parallel to the fluid channel, but now offset along the channel boundary.

The velocity of the captured particles after FIDT deactivation was calculated to be 251.57 $\mu m/s$, which is again significantly lower than the maximum flow velocity measured for 48-hpf zebrafish embryos reported in literature [40].

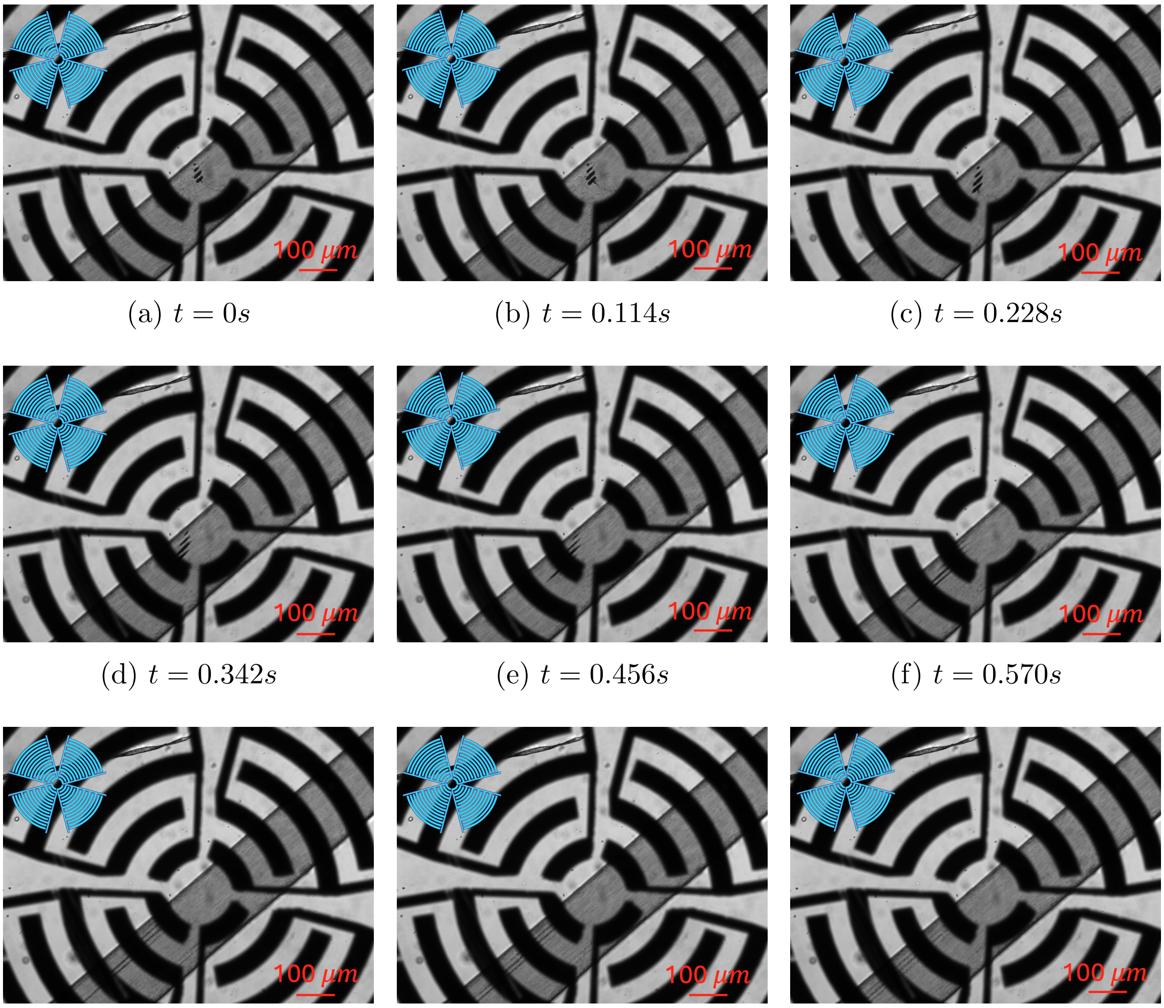

(a) $t = 0s$ (b) $t = 0.114s$ (c) $t = 0.228s$

(d) $t = 0.342s$ (e) $t = 0.456s$ (f) $t = 0.570s$

(g) $t = 0.684s$ (h) $t = 0.798s$ (i) $t = 0.912s$

Figure 4.5: Time-sequential visualization of PS particles, initially captured at a offset, being displaced and carried away by the fluid flow, upon deactivation of the FIDT. The width of the channel was 300 μm and the height was $240\mu m$.

The same procedure was repeated using yeast cells, and the results were similarly successful for the centered and misaligned channel setup, as shown in Fig. 4.6. The velocity of yeast cells after FIDT deactivation was calculated to be 368.49 $\mu m/s$, again significantly slower than the velocities in zebrafish vessels reported in the literature [40].

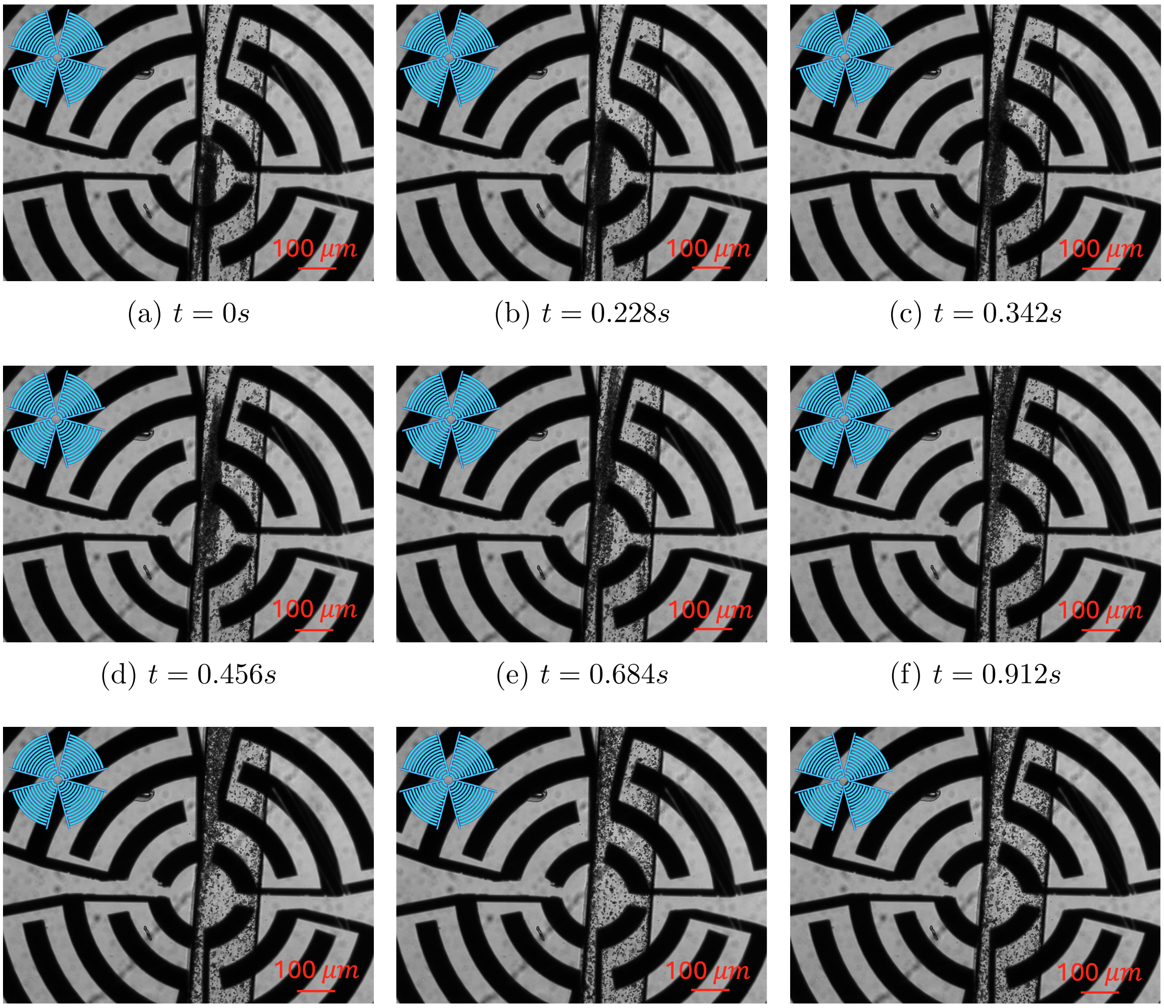

(a) $t = 0s$ (b) $t = 0.228s$ (c) $t = 0.342s$

(d) $t = 0.456s$ (e) $t = 0.684s$ (f) $t = 0.912s$

(g) $t = 2.166s$ (h) $t = 4.446s$ (i) $t = 6.042s$

Figure 4.6: Time-sequential visualization of yeast cells, initially captured, being displaced and carried away by the fluid flow, upon deactivation of the FIDT. The width of the channel was 300 μm and the height was 240μm.

Finally, the experiments were also repeated with microbubbles. The conditions were slightly different from the experiments with PS particles and yeast cells, as a channel with a diameter of approximately 50 μm was used to more closely mimic the dimensions of the zebrafish's dorsal aorta, which measures approximately 36 μm [39]. Under these conditions, it was possible to capture the microbubbles using a frequency of 39.2 MHz. However, since microbubbles have a negative ACF, they migrated to the walls of the channel upon FIDT activation because the antinodes of the acoustic standing wave are located at the channel boundaries. Clusters of microbubbles initially captured in the center of the channel were observed to gradually migrate to the walls of the channel over time, as indicated by the red arrows in Fig. 4.7.

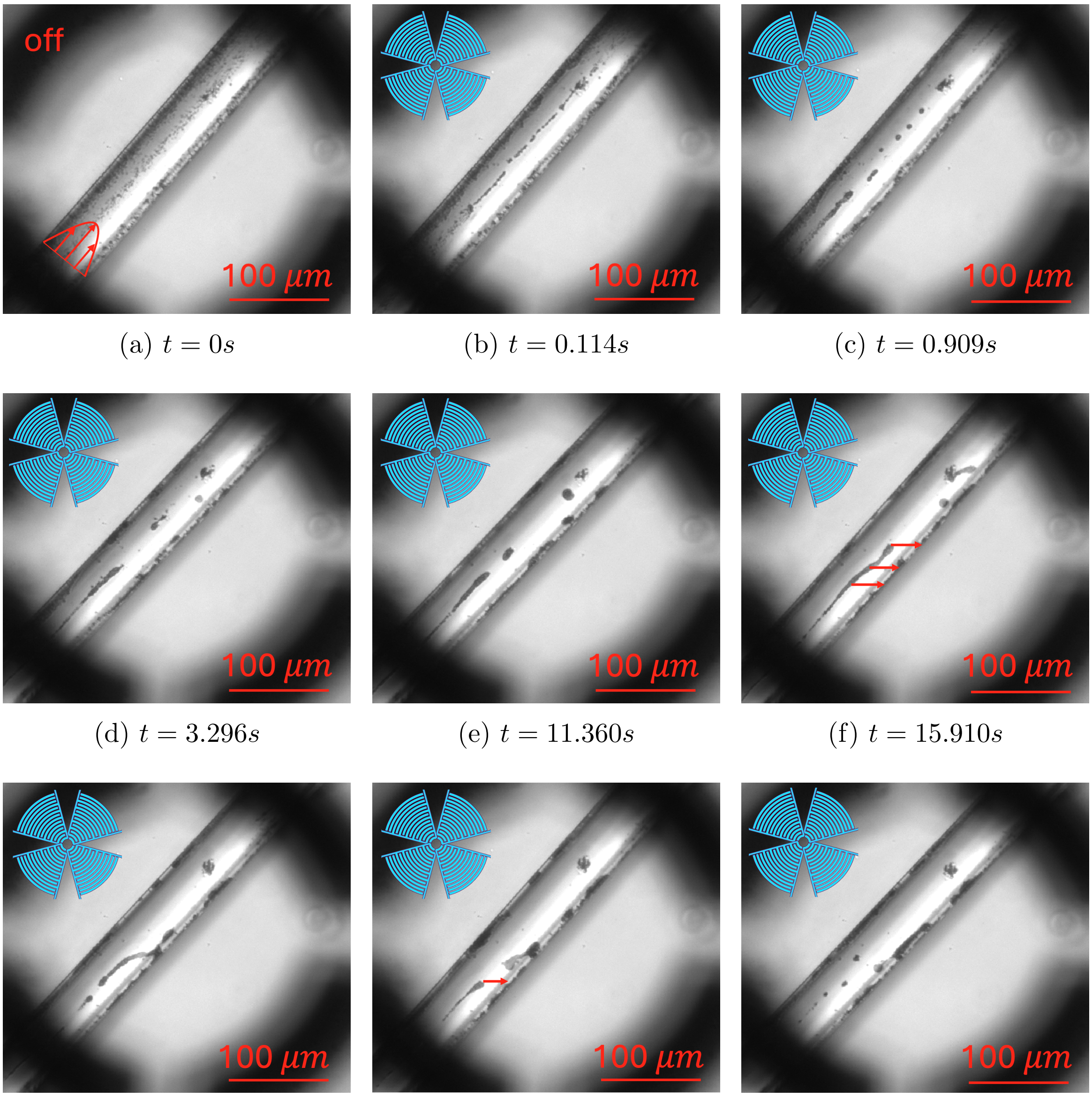

(a) $t = 0s$ (b) $t = 0.114s$ (c) $t = 0.909s$

(d) $t = 3.296s$ (e) $t = 11.360s$ (f) $t = 15.910s$

(g) $t = 18.178s$ (h) $t = 20.904s$ (i) $t = 24.086s$

Figure 4.7: Time-sequential visualization of microbubbles captured at the walls of the channel after FIDT actuation, under controlled fluid flow conditions. The width of the channel was 50 μm and the height was 30 μm.

4.3 Manipulation of Microbubbles in Zebrafish Embryos

The yolk of the zebrafish embryo is a nutrient-rich part of the embryo that provides essential resources to the developing embryo[49]. This cavity was the site of injection for fluorescent microbubbles, resulting in their accumulation in this area, as can be seen in Fig. 4.8. Furthermore, the large cavity and slow background streaming provided favorable conditions for manipulating the microbubble clusters, which is highlighted in Fig. 4.9 by the red arrow. The cluster of microbubbles was observed to move upon FIDT actuation, and by sweeping the frequency around the resonance frequency of 59.2 MHz, the cluster could be moved around. However, the movement was not precise and it was not possible to control a desired trajectory of the cluster.

The movement of the particles was probably primarily due to acoustic streaming, generated by the FIDT, since significant streaming motion could be observed. This manipulation of was successfully reproduced using red fluorescent microbubbles, as shown in Fig. A.4 in the Appendix.

The velocity of the microbubbles in the main vessel, the dorsal aorta, was calculated to be 2690 $\mu m/s$, whereas the velocity in the cavity of the yolk was measured to be much lower at 625 $\mu m/s$. Velocity was measured and calculated as described in Chapter 3.4.

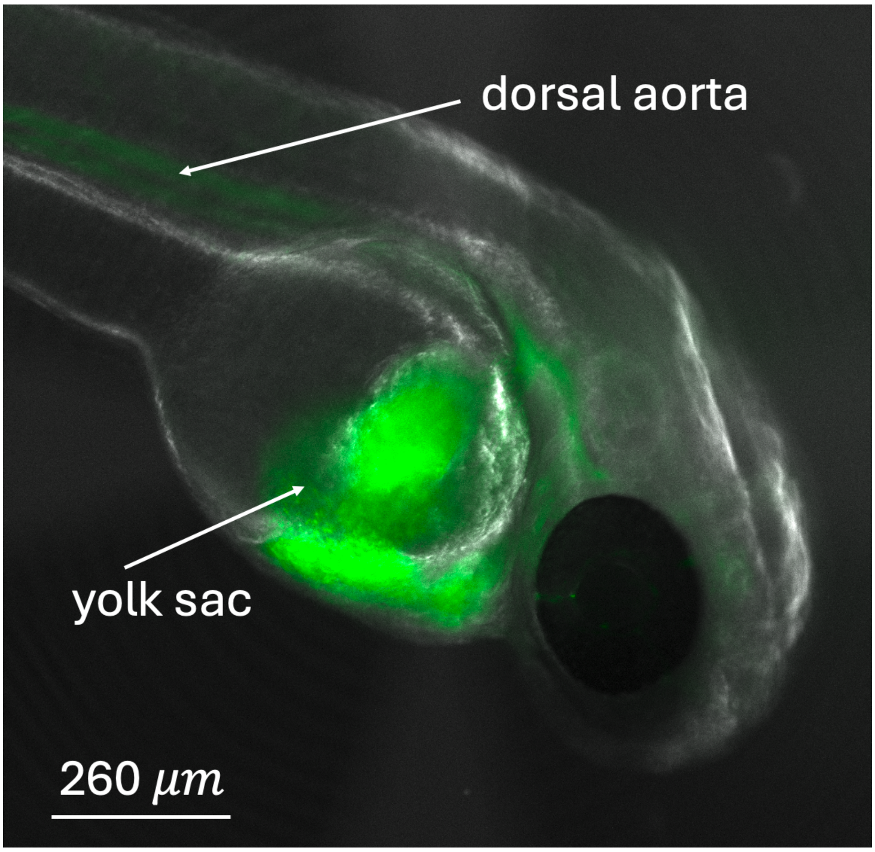

Figure 4.8: Zebrfafish under the fluoresent microscope

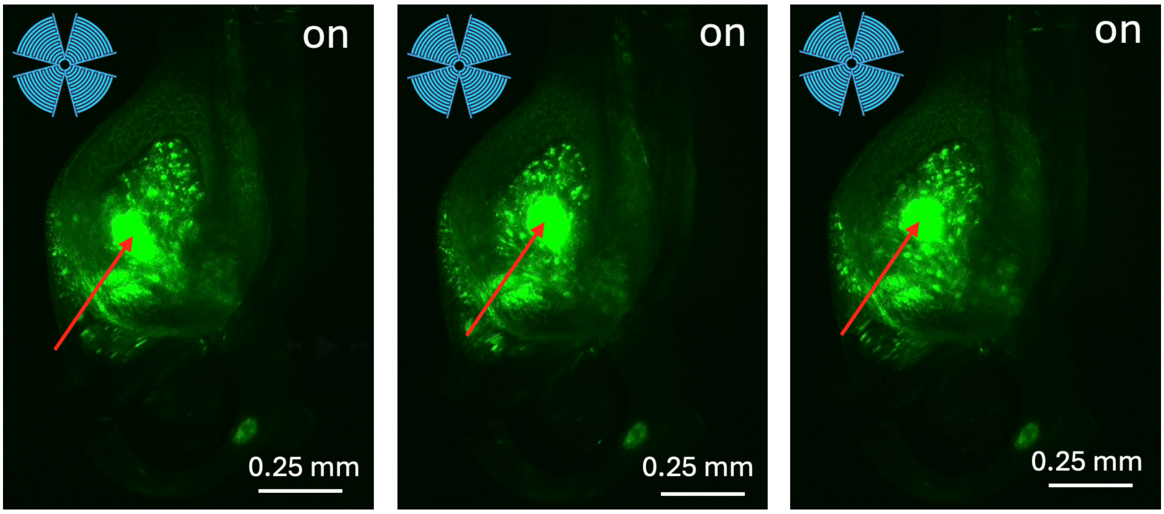

(a) $t = 0s$ (b) $t = 8s$ (c) $t = 16s$

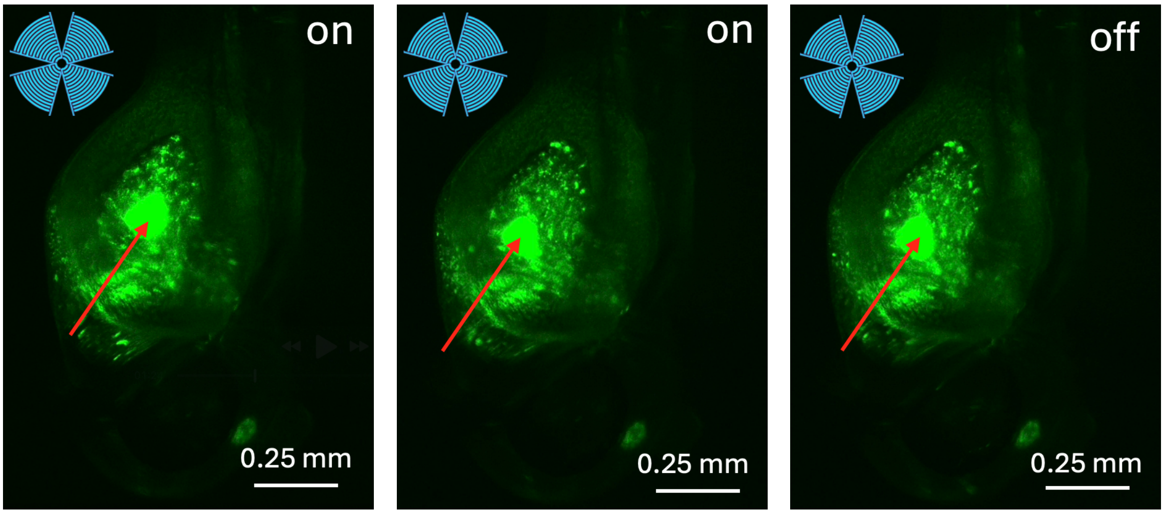

(d) $t = 24s$ (e) $t = 32s$ (f) $t = 36s$

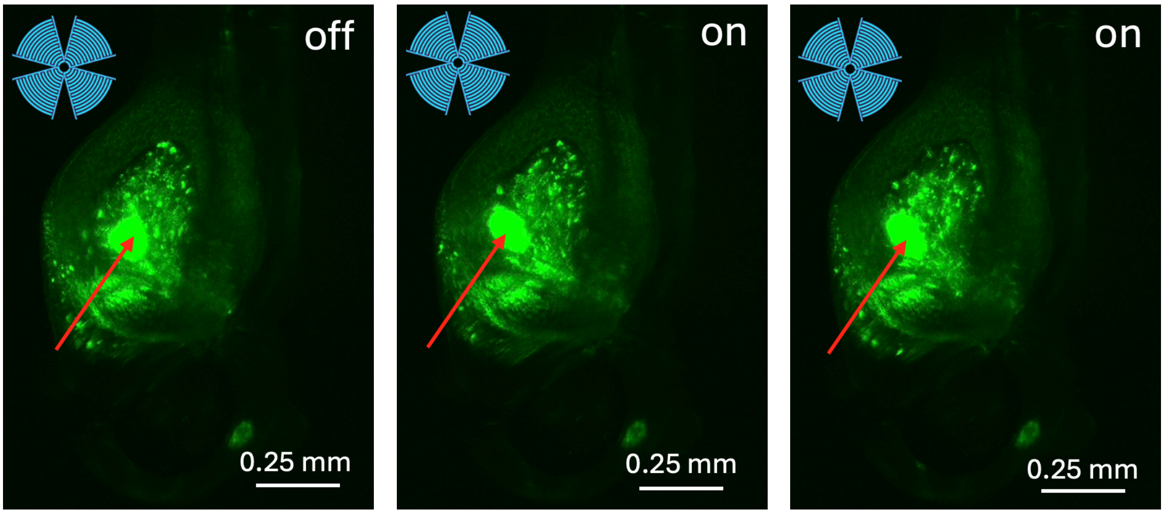

(g) $t = 39s$ (h) $t = 42s$ (i) $t = 45s$

Figure 4.9: Manipulation of green fluorescent microbubbles in the yolk sac of a zebrafish embryo using the FIDT with a resonance frequency of approximately 59.2 MHz.

In the same cavity as shown in Fig. 4.9, and at the same resonance frequency of 59.3 MHz, a straight line pattern was achieved by activating only one pair of opposing FIDTs, as depicted in Fig. 4.10. The pattern could still be formed despite the relatively high fluid velocity of $625\mu m/s$ was present.

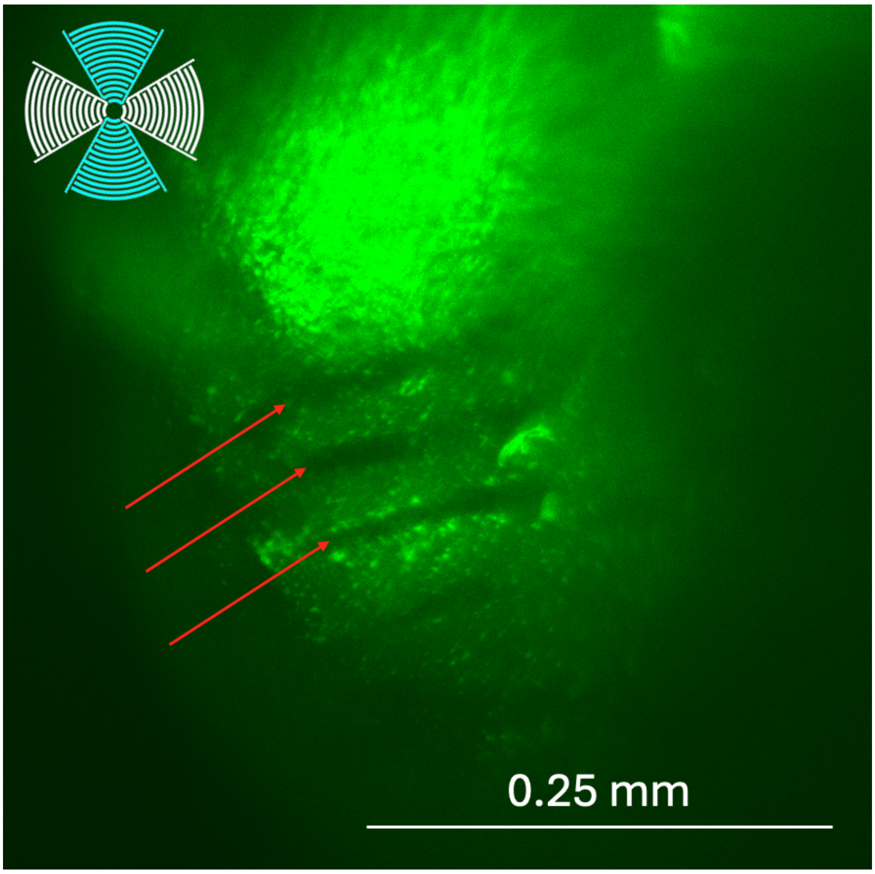

Figure 4.10: Pattern of parallel lines in the zebrafish's yolk sac, indicated by the red arrows.

Chapter 5

Discussion

The objective of this bachelor's thesis was to achieve *in vivo* particle trapping and manipulation within the vasculature of zebrafish embryos. As a preparatory step, *in vitro* experiments were conducted to characterize IDTs and simulate the vessel using microfluidic channels.

5.1 *In Vitro* Experiments

The *in vitro* trials were very promising, as particle trapping and manipulation were successfully achieved under various conditions.

5.1.1 *In Vitro* Experiments under Static Conditions

Static conditions without fluid flow produced the most favorable outcomes. Using FIDTs with an individual electrode width of $50\mu m$ and using PS particles, the experiments demonstrated that it is possible to capture a cluster of particles in a single dot of the focal point of the FIDT. This was achieved at a resonance frequency of approximately 39 MHz. Additionally, it was shown that by slightly adjusting the frequency around the resonance frequency, deformation of the particle cluster could be achieved.

At the higher harmonic of approximately 59 MHz, the cluster could not be formed as homogeneously as at 39 MHz, and a higher order pattern, with multiple pressure nodes at the focal point was observed. Even higher resonance frequencies could not be determined, as the function generator in this project was limited to 60 MHz.

5.1.2 *In Vitro* Experiments under Non-Static Conditions

Under conditions with non-zero fluid velocity, the results deviated from the desired outcomes. PS particles trapped at the focal point of the same FIDT, as mentioned above, experienced elongation along the channel direction, forming a striped accumulation pattern. This phenomenon likely resulted from the interaction of two factors. First, trapping was only possible at approximately 59 MHz, the frequency at which a higher harmonic pattern, with multiple pressure nodes at the focal point, was observed in the absence of fluid flow. Second, the background fluid flow introduced a drag force, which stretched the preexisting checkered pattern along the channel direction. The combined effects of acoustic trapping and drag force appear to have caused the observed striped accumulation pattern. Furthermore, the trapping phenomenon was observed at two distinct heights within the channel, raising important questions regarding the controlled positioning of the FIDT's focal point along the z-axis, perpendicular to the plane of the FIDT. This was probably observed because of the effects of the higher harmonic, which also introduces stronger streaming.

It was not possible to trap the PS particles at the lower resonance frequency of approximately 39 MHz, as the power of the SAW was probably insufficient to counteract the increased drag force induced by the background fluid flow. The power scales with the square of the voltage, but even with increased voltage, trapping at approximately 39 MHz could not be achieved.

5.2 *In Vivo* Experiments

The *in vivo* experiments encountered several difficulties and sources of error, as the environment of a living creature introduces a lot more complexity.

5.2.1 Fast Fluid Flow in Comparison to *In Vitro* Simulations

The measured velocities of the particles in the dorsal aorta of the zebrafish were an order of magnitude higher than those observed during the *in vitro* trials, where conditions in the zebrafish were simulated, as shown in Fig. 5.1. Additionally, the calculated velocity of the microbubbles in the zebrafish vessel represents an average velocity, as the blood flow is not steady and accelerates and decelerates substantially. Thus, the velocity of blood flow in the main vessel of zebrafish was even higher for short periods of time, with peak velocities measured at up to $5800\mu m/s$, more than ten times the maximum velocity calculated in the *in vitro* trials of $400.16\mu m/s$, while the lower limit of the flow velocity in the dorsal aorta of zebra fish found in the literature was approximately at $1200\mu m/s$ [40]. This very wide range of velocities in the dorsal aorta of zebrafish could be an explanation for why it was possible to trap particles under simulated conditions in the *in vitro* experiments but not in the main vessel (dorsal aorta) during the *in vivo* experiments. The highest measured velocity at which particle manipulation could still be observed, was at 600 $\mu m/s$ in the yolk of zebrafish. Based on the data collected in this project, only an approximate range for the critical flow velocity threshold can be inferred for successful particle trapping, estimated between 625 $\mu m/s$ and 2690 $\mu m/s$.

5.2.2 Trapping in Narrow Vessels

The capture and manipulation of particles in the narrow blood vessels of zebrafish proved to be challenging. Successful trapping and manipulation were achieved exclusively in the larger cavities of the zebrafish's vasculature, such as the yolk sac, where manipulation could be clearly demonstrated. One potential reason for this difficulty could be the density of the fluorescent particles used. Their higher density (approx. 1.05 g/cm^3), compared to the density of blood plasma (approx. $1.025g/cm^3$) [48], probably caused them to sediment rather than remain suspended, preventing them from circulating in the zebrafish vasculature [50]. Additionally, the surface properties of the fluorescent particles may have interacted unfavorably with the rough wall of the blood vessel, potentially leading to adhesion or entrapment of the particles in the wall. The fluorescent particles are not deformable, which could have led to a lack of flexibility to navigate the narrow and dynamic environment of the blood vessels.

To address the density-related issue, fluorescent microbubbles were employed, as they have a lower density compared to blood components and have been successfully trapped in previous work using BAWs [11]. Additionally, the deformable nature of

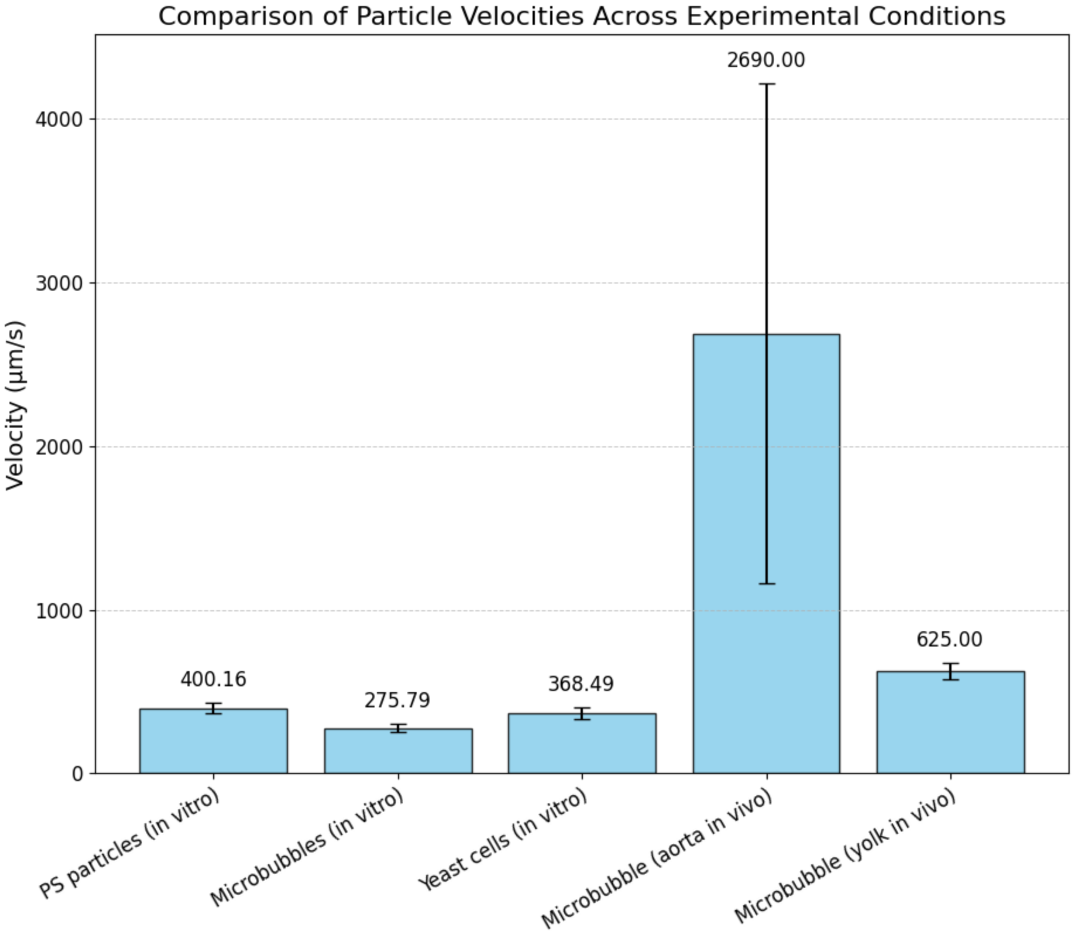

Figure 5.1: Particle velocities (in vitro) with controlled fluid flow compared to the velocity of microbubbes during in vivo trials in the zebrafish's dorsal aorta and yolk. The error bars represent lowest and highest velocities measured or found in literature for each particle (they do not represent mathematical standard deviations).

microbubbles could be an advantage of the non-deformable fluorescent particles. However, similar to the fluorescent particles used previously, microbubble manipulation was only effective in the larger cavities. Efforts to enhance the trapping of microbubbles in smaller vessels by increasing the voltage amplitude failed. Furthermore, there was an upper limit to the applied voltage, as the zebrafish's heart rate became critically fast at voltages near 1.4 V_{pp} (multiplied by the factor 15 by the gain of the amplifier) and stopped entirely at higher voltages. It is also possible that the IDT's focal point was not aligned with the main vessel, as alignment is difficult to control.

5.2.3 Adjustability of the Focal Point Height of FIDT's

As described in Chapter 2.1.7, SAWs only propagate along the substrate surface. For this reason, it is challenging to arbitrarily adjust the position of the FIDT's focal point in the z-direction, perpendicular to the IDT plane. It was observed that increasing the amplitude caused the z-position of the FIDT's focal point to shift away from the device, but this is likely due to stronger streaming and cannot be controlled precisely. This issue is particularly problematic in a the *in vivo* experiments, as zebrafish embryos do not have uniform dimensions, and the relative height of the vessels to the FIDT can vary depending on the orientation of the zebrafish and how the embryo is embedded in the agarose gel.

5.2.4 Fluorescence Spectra Mismatch

The fluorescent particles initially used emitted light in the red spectrum and not in the green spectrum, as was expected. This caused overlap with the genetically induced red fluorescence of the zebrafish, making it difficult to distinguish particles. Particles emitting in the green spectrum would have provided better contrast, enabling clearer visualization of the particles during experiments.

Chapter 6

Conclusion & Outlook

The manipulation of microparticles utilizing SAW devices has shown promising results but requires further investigation. In particular, the *in vivo* trials should be repeated and extensively optimized, as these experiments still contain significant uncertainties that need to be studied more rigorously to ensure reliable and reproducible results of trapping and manipulating of particles in blood vessels. If particle trapping and manipulation within zebrafish vessels could be reliably demonstrated and a method for adjusting the height of the IDT's focal point is developed, this technology could enable a variety of promising applications.

6.1 Optimization for Future Research

During this project, various areas of improvement were identified, and in the following section recommendations are provided to address these aspects.

6.1.1 Enhancing *In Vitro* Simulation of Blood Vessels

The *in vitro* setup could be further optimized to better simulate conditions in blood vessels. One recommendation is to connect a pump to a microfluidic channel to precisely control the fluid velocity and match the *in vivo* conditions. With this setup, it would be beneficial to determine the maximum blood flow velocity, at which it is still possible to capture and manipulate particles.

Furthermore, a fluid with viscosity similar to blood could be used to better replicate the actual *in vivo* environment.

6.1.2 Addressing the Challenge of Limited Vertical Adjustability of the IDT Focal Point

To manipulate particles not only in a 2D plane but also in 3D, future work must address the issue of limited resolution along the z-axis (perpendicular to the IDT plane). The lack of control in the z-direction currently restricts the broader applicability of SAW devices. This challenge highlights the need for technological advancements that enable more precise particle manipulation in three dimensions.

6.1.3 Systematic Repetition of Experiments and Interdisciplinary Collaboration

The blood vessel environment introduces many more uncertainties compared to *in vitro* trials with microfluidic channels. Factors such as flow velocity, unsteady flow, rough vessel walls, and variations in particle size and density create significant challenges. To minimize these uncertainties, *in vivo* experiments should be repeated systematically. Collaboration with biologists and physicists specializing in this area would be highly beneficial for refining the experimental setup and addressing potential errors.

Furthermore, investigating particle behavior beyond the frequency range tested in this project could yield additional insights.

6.1.4 Exploring Use of Younger or Older Zebrafish Embryos

Blood flow velocity increases until the zebrafish reach 3-dpf, as shown in the theoretical background on zebrafish embryos [40]. Thus, to reduce the effects of drag force caused by high blood flow velocities, experiments could be conducted with zebrafish embryos at 24-hpf or at 4-dpf. This could enable more stable experimental conditions.

6.2 Possible Future Applications

Addressing the aforementioned challenges could pave the way for the potential applications discussed in the following section.

6.2.1 Enhanced Targeted Drug Delivery

More precise trapping of microbubbles or ultrasound-responsive polymer vesicles within blood vessels could significantly improve targeted drug delivery. By combining FIDTs and TSAW devices, microbubbles could be trapped at specific vascular sites. Subsequent ultrasound-mediated destruction of microbubbles by a TSAW device could improve localized drug release, thereby increasing therapeutic efficacy [51], [52], [53].

6.2.2 Vessel Occlusion for Tumor Treatment

Occluding blood vessels that supply tumors with nutrients and oxygen has been shown to inhibit tumor growth. If it is shown, that FIDTs can reliably form sufficiently larger particle clusters to stop blood flow in vessels, this could be a promising non-invasive treatment. Currently, this approach is achievable only through High-Intensity Focused Ultrasound (HIFU) [54].

6.2.3 Clotting of Bioparticles for Hemophilia Treatment and Wound Healing

Effective wound healing requires the formation of blood clots to prevent excessive bleeding and to facilitate tissue regeneration. FIDTs could accelerate or enhance the clotting process by capturing platelets and facilitate their aggregation at the wound site [55]. For patients with hemophilia, this could offer a non-invasive alternative to traditional treatments [56].

References

[1] Martin Wiklund. Acoustofluidics 12: Biocompatibility and cell viability in microfluidic acoustic resonators. *Lab on a Chip*, 12(11):2018–2028, 5 2012.

[2] Andreas Lenshof, Carl Johannesson, Mikael Evander, Johan Nilsson, and Thomas Laurell. Acoustic Cell Manipulation. *Part of the book series: Microsystems and Nanosystems*, pages 129–173, 2017.

[3] Ghulam Destgeer and Hyung Jin Sung. Recent advances in microfluidic actuation and micro-object manipulation via surface acoustic waves. *Lab on a Chip*, 15(13):2722–2738, 6 2015.

[4] Reza Rasouli, Karina Martinez Villegas, and Maryam Tabrizian. Acoustofluidics – changing paradigm in tissue engineering, therapeutics development, and biosensing. *Lab on a Chip*, 23(5):1300–1338, 3 2023.

[5] Xuejia Hu, Jingjing Zheng, Qinghao Hu, Li Liang, Dongyong Yang, Yanxiang Cheng, Sen Sen Li, Lu Jian Chen, and Yi Yang. Smart acoustic 3D cell construct assembly with high-resolution. *Biofabrication*, 14(4):045003, 7 2022.

[6] A. Ashkin, J. M. Dziedzic, J. E. Bjorkholm, and Steven Chu. Observation of a single-beam gradient force optical trap for dielectric particles. *Optics Letters, Vol. 11, Issue 5, pp. 288-290*, 11(5):288–290, 5 1986.

[7] Adem Ozcelik, Joseph Rufo, Feng Guo, Yuyang Gu, Peng Li, James Lata, and Tony Jun Huang. Acoustic tweezers for the life sciences. *Nature Methods 2018 15:12*, 15(12):1021–1028, 11 2018.

[8] José L. Pons. Emerging Actuator Technologies: A Micromechatronic Approach. *Emerging Actuator Technologies: A Micromechatronic Approach*, pages 1–278, 6 2005.

[9] A. Lenshof, M. Evander, T. Laurell, and J. Nilsson. Acoustofluidics 5: Building microfluidic acoustic resonators. *Lab on a Chip*, 12(4):684–695, 1 2012.

[10] Heba Ahmed, Shwathy Ramesan, Lillian Lee, Amgad R. Rezk, and Leslie Y. Yeo. On-Chip Generation of Vortical Flows for Microfluidic Centrifugation. *Small*, 16(9):1903605, 3 2020.

[11] Viktor Manuel Jooss, Jan Stephan Bolten, Jörg Huwyler, and Daniel Ahmed. In vivo acoustic manipulation of microparticles in zebrafish embryos. *Science Advances*, 8(12), 3 2022.

[12] Michael Baudoin, Jean Louis Thomas, Roudy Al Sahely, Jean Claude Gerbedoen, Zhixiong Gong, Aude Sivery, Olivier Bou Matar, Nikolay Smagin, Peter Favreau, and Alexis Vlandas. Spatially selective manipulation of cells with single-beam acoustical tweezers. *Nature Communications 2020 11:1*, 11(1):1–10, 8 2020.

[13] James Friend and Leslie Y. Yeo. Microscale acoustofluidics: Microfluidics driven via acoustics and ultrasonics. *Reviews of Modern Physics*, 83(2):647, 6 2011.

[14] Yiming Li, Dongfang Liang, Alexandre Kabla, Yuning Zhang, and Xin Yang. Sensitivity of acoustofluidic particle manipulation to microchannel height in standing surface acoustic wave-based microfluidic devices. *Physics of Fluids*, 35(12):122018, 12 2023.

[15] Mercedes Stringer, Ziming Zeng, Xiaoyan Zhang, Yanyan Chai, Wen Li, Jikai Zhang, Huiling Ong, Dongfang Liang, Jing Dong, Yiming Li, Yongqing Fu, and Xin Yang. Methodologies, technologies, and strategies for acoustic streaming-based acoustofluidics. *Applied Physics Reviews*, 10(1), 3 2023.

[16] Alex D.D. Craik. Lord Kelvin on fluid mechanics. *The European Physical Journal H 2012 37:1*, 37(1):75–114, 5 2012.

[17] Martin Wiklund, Roy Green, and Mathias Ohlin. Acoustofluidics 14: Applications of acoustic streaming in microfluidic devices. *Lab on a Chip*, 12(14):2438–2451, 6 2012.

[18] Carl Eckart. Vortices and Streams Caused by Sound Waves. *Physical Review*, 73(1):68, 1 1948.

[19] Wei Wei, Yaping Wang, Zhaoxun Wang, and Xuexin Duan. Microscale acoustic streaming for biomedical and bioanalytical applications. *TrAC Trends in Analytical Chemistry*, 160:116958, 3 2023.

[20] Rune Barnkob and Henrik Bruus. Acoustofluidics: Theory and simulation of radiation forces at ultrasound resonances in microfluidic devices. *Proceedings of Meetings on Acoustics*, 6(1), 5 2009.

[21] Lev P Gor'kov. Selected Papers of Lev P Gor'kov. *Selected Papers of Lev P Gor'kov*, 11 2014.

[22] Anand Pai, Chandrakant R. Kini, and Satish Shenoy B. Development of materials and structures for shielding applications against Blast and Ballistic impact: A Detailed Review. *Thin-Walled Structures*, 179, 10 2022.

[23] Frank Fahy. Impedance. *Foundations of Engineering Acoustics*, pages 48–73, 1 2001.

[24] Steven L. Garrett. Reflection, Transmission, and Refraction. pages 513–542, 2020.

[25] Yuan Gao, Mengren Wu, Yang Lin, and Jie Xu. Acoustic Microfluidic Separation Techniques and Bioapplications: A Review. *Micromachines 2020, Vol. 11, Page 921*, 11(10):921, 10 2020.

[26] M. A. Faridi, H. Ramachandraiah, I. Iranmanesh, D. Grishenkov, M. Wiklund, and A. Russom. MicroBubble activated acoustic cell sorting. *Biomedical Microdevices*, 19(2):1–7, 6 2017.

[27] Andreas Lenshof and Thomas Laurell. Acoustophoresis. *Encyclopedia of Nanotechnology*, pages 1–6, 2015.

[28] Nino F. Läubli, Michael S. Gerlt, Alexander Wüthrich, Renard T.M. Lewis, Naveen Shamsudhin, Ulrike Kutay, Daniel Ahmed, Jürg Dual, and Bradley J. Nelson. Embedded Microbubbles for Acoustic Manipulation of Single Cells and Microfluidic Applications. *Analytical Chemistry*, 93(28):9760–9770, 7 2021.

[29] Citsabehsan Devendran, David J. Collins, and Adrian Neild. The role of channel height and actuation method on particle manipulation in surface acoustic wave (SAW)-driven microfluidic devices. *Microfluidics and Nanofluidics*, 26(2):1–14, 2 2022.

[30] Mengxi Wu, Kejie Chen, Shujie Yang, Zeyu Wang, Po Hsun Huang, John Mai, Zeng Yao Li, and Tony Jun Huang. High-throughput cell focusing and separation via acoustofluidic tweezers. *Lab on a Chip*, 18(19):3003–3010, 9 2018.

[31] Shuren Song, Qi Wang, Jia Zhou, and Antoine Riaud. Design of interdigitated transducers for acoustofluidic applications. *Nanotechnology and Precision Engineering*, 5(3), 9 2022.

[32] R. M. White and F. W. Voltmer. DIRECT PIEZOELECTRIC COUPLING TO SURFACE ELASTIC WAVES. *Applied Physics Letters*, 7(12):314–316, 12 1965.

[33] An Huang, William Connacher, Mark Stambaugh, Naiqing Zhang, Shuai Zhang, Jiyang Mei, Aditi Jain, Sravya Alluri, Vincent Leung, Anushi E. Rajapaksa, and James Friend. Practical microcircuits for handheld acoustofluidics. *Lab on a Chip*, 21(7):1352–1363, 4 2021.

[34] Ruijian Zhu and Zengmei Wang. Piezoelectric one- to two-dimensional nanomaterials for vibration energy harvesting devices. *Emerging 2D Materials and Devices for the Internet of Things*, pages 221–241, 2020.

[35] Patrick M. Winter, Gregory M. Lanza, Samuel A. Wickline, Marc Madou, Chunlei Wang, Parag B. Deotare, Marko Loncar, Yoke Khin Yap, Jérôme Rose, Mélanie Auffan, Olivier Proux, Vincent Niviere, Jean-Yves Bottero, Zhong Lin Wang, Ying Liu, R. G. Polcawich, J. S. Pulskamp, R. M. Proie, Woo-Tae Park, Sergei V. Kalinin, Brian J. Rodriguez, Andrei L. Kholkin, Gang Logan Liu, Jao Lagemaat, Lorenzo Valdevit, John W. Hutchinson, Seajin Oh, Marc Madou, Katja Tonisch, Enrica De Rosa, Joseph Fernandez-Moure, Ennio Tasciotti, Denis Gebauer, Brian E. O'Neill, and King C. Li. Piezoelectric Effect at Nanoscale. *Encyclopedia of Nanotechnology*, pages 2085–2099, 2012.

[36] Huseyin Enes Salman and Huseyin Cagatay Yalcin. Advanced blood flow assessment in Zebrafish via experimental digital particle image velocimetry and computational fluid dynamics modeling. *Micron*, 130:102801, 3 2020.

[37] Narendra H. Pathak and Michael J.F. Barresi. Zebrafish as a Model to Understand Vertebrate Development. *The Zebrafish in Biomedical Research: Biology, Husbandry, Diseases, and Research Applications*, pages 559–591, 1 2020.

[38] Alvin C.H., Yuhan Guo, Alex B.L., and Anskar Y.H. Modeling Tumor Angiogenesis with Zebrafish. *Vasculogenesis and Angiogenesis - from Embryonic Development to Regenerative Medicine*, 11 2011.

[39] Dmitrii Chalin, Andrei Nikolaev, Evgeniy Sadyrin, Karima Kissa, and Ivan Golushko. Simple Coarse-Grained Model of the Zebrafish Embryonic Aorta Suggesting the Mechanism Driving Shape Changes During Stem Cell Production. *Advanced Structured Materials*, 195:59–68, 2023.

[40] Fiorency Santoso, Bonifasius Putera Sampurna, Yu Heng Lai, Sung Tzu Liang, Erwei Hao, Jung Ren Chen, and Chung Der Hsiao. Development of a Simple ImageJ-Based Method for Dynamic Blood Flow Tracking in Zebrafish Embryos and Its Application in Drug Toxicity Evaluation. *Inventions 2019, Vol. 4, Page 65*, 4(4):65, 11 2019.

[41] LiNbO3 Properties.

[42] Jiyang Mei, Naiqing Zhang, and James Friend. Fabrication of Surface Acoustic Wave Devices on Lithium Niobate. *JoVE (Journal of Visualized Experiments)*, 2020(160):e61013, 6 2020.

[43] Scintica Website. Microbubbles – Scintica, 2024.

[44] Leah M. Johnson, Lu Gao, C. Wyatt Shields, Margret Smith, Kirill Efimenko, Kevin Cushing, Jan Genzer, and Gabriel P. López. Elastomeric microparticles for acoustic mediated bioseparations. *Journal of Nanobiotechnology*, 11(1):1–8, 6 2013.

[45] Jeremy J. Ramsden. Forces at the nanoscale. *Nanotechnology*, pages 41–60, 1 2016.

[46] Technical Page - Characteristics of Polystyrene Particles - Spherotech.

[47] Fluorescent Green Polyethylene Microspheres, Beads, Particles - Density 1.025g/cc - Bright Green Polymer MicroBeads Diameter 10micron to 1mm.

[48] Adriana Gaia Cairelli, Renee Wei Yan Chow, Julien Vermot, and Choon Hwai Yap. Fluid mechanics of the zebrafish embryonic heart trabeculation. *PLOS Computational Biology*, 18(6):e1010142, 6 2022.

[49] Lilianna Solnica-Krezel and Wolfgang Driever. Microtubule arrays of the zebrafish yolk cell: organization and function during epiboly. *Development*, 120(9):2443–2455, 9 1994.

[50] Q. Xu. Microinjection into zebrafish embryos. *Methods in molecular biology (Clifton, N.J.)*, 127:125–132, 1999.

[51] Long Meng, Feiyan Cai, Peng Jiang, Zhiting Deng, Fei Li, Lili Niu, Yan Chen, Junru Wu, and Hairong Zheng. On-chip targeted single cell sonoporation with microbubble destruction excited by surface acoustic waves. *Applied Physics Letters*, 104(7), 2 2014.

[52] Lauren J. Delaney, Selin Isguven, John R. Eisenbrey, Noreen J. Hickok, and Flemming Forsberg. Making waves: how ultrasound-targeted drug delivery is changing pharmaceutical approaches. *Materials Advances*, 3(7):3023–3040, 4 2022.

[53] J. Angel Navarro-Becerra and Mark A. Borden. Targeted Microbubbles for Drug, Gene, and Cell Delivery in Therapy and Immunotherapy. *Pharmaceutics 2023, Vol. 15, Page 1625*, 15(6):1625, 5 2023.

[54] Jordan B. Joiner, Yuliya Pylayeva-Gupta, and Paul A. Dayton. Focused Ultrasound for Immunomodulation of the Tumor Microenvironment. *The Journal of Immunology*, 205(9):2327–2341, 11 2020.

[55] Biao Cheng and Xiaobing Fu. Biologic Transducers in Wound Healing. *Chronic Wound Management*, pages 77–106, 2023.

[56] A. Tanaka and K. Fukutake. Hemophilia A. *Ryōikibetsu shōkōgun shirīzu*, (21 Pt 2):423–426, 1 1998.

Appendix A

Additional Results

A.1 Additional IDT characterization results

A.1.1 FIDT with Electrode Width of 25 μm:

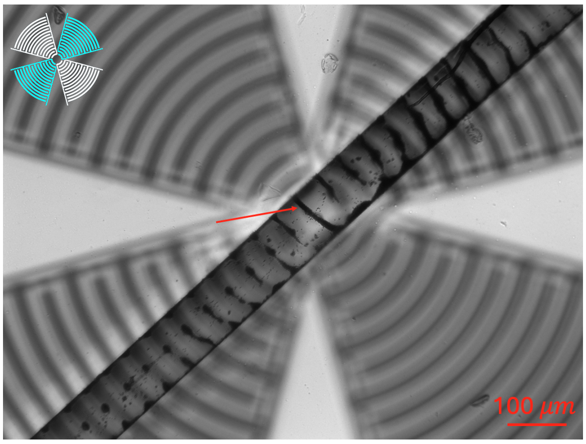

Figure A.1: Upon activation of just one pair of opposing FIDT sections (resonance frequency of 44.7 MHz, a straight line pattern was formed. The channel width was 100μm and the height was 30μm.

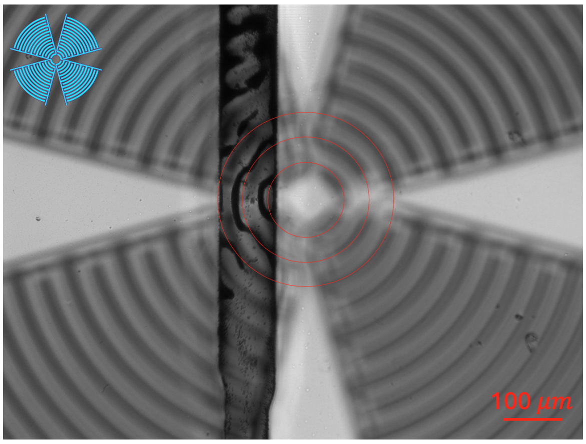

Figure A.2: Upon activation of all four IDT sections (resonance frequency of 42.2 MHz), and deliberate channel offsetting, the particles aligned precisely along the curved pressure nodes, effectively reproducing the spatial pattern of the FIDT. The width of the channel was 100 μm and and the height was 30μm

A.1.2 Straight IDT with Electrode Width of 50 μm:

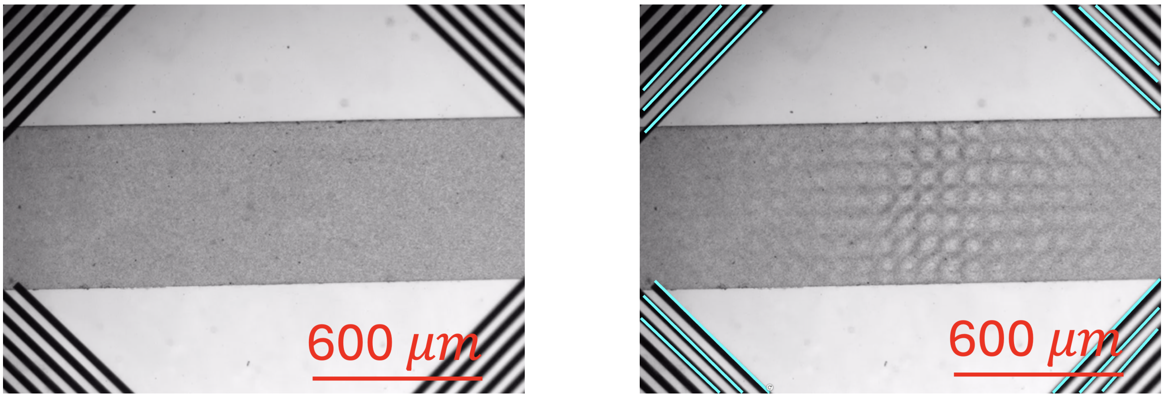

(a) $t = 0s$

(b) $t = 5s$

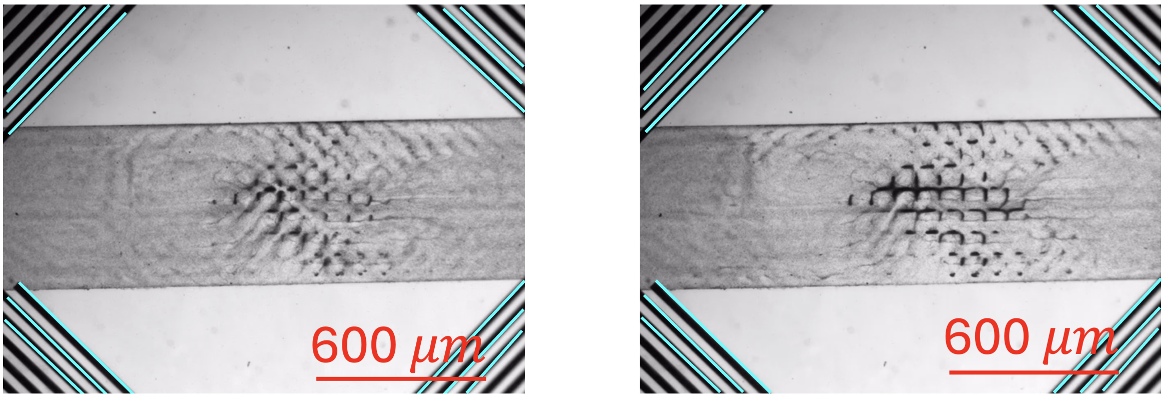

(c) $t = 30s$

(d) $t = 70s$

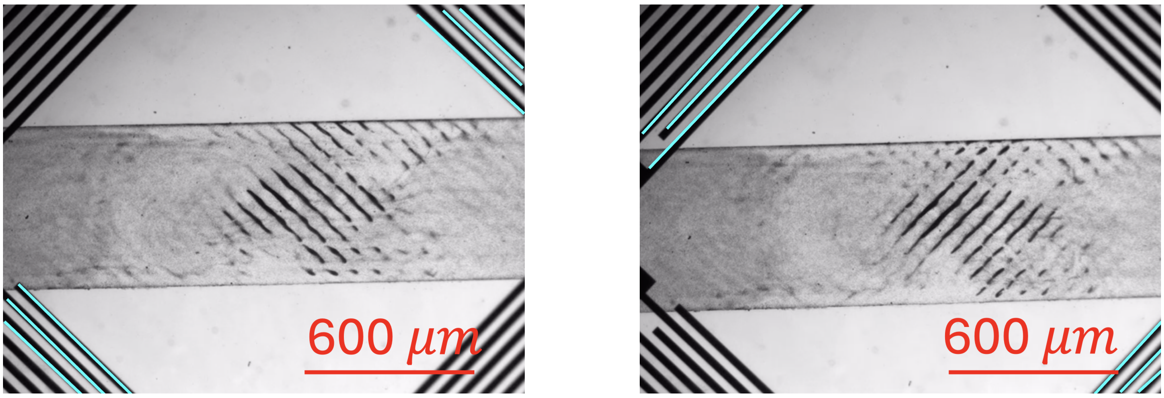

(e) $t = 106s$

(f) $t = 123s$

Figure A.3: Patterning of polystyrene particles using a straight IDT with 4 sections. Actuating all four IDTs (resonance frequency of 18.4 MHz), results in a checkered pattern, while actuating just one pair of IDTs, results in line patterns in the same orientation as the actuated IDT sections. The channel width was 600 μm and the height was 240 μm. Electrodes colored in blue indicate activated IDTs.

A.2 Results of Repeated Manipulation of Microbubbles in Zebrafish's Yolk Sac

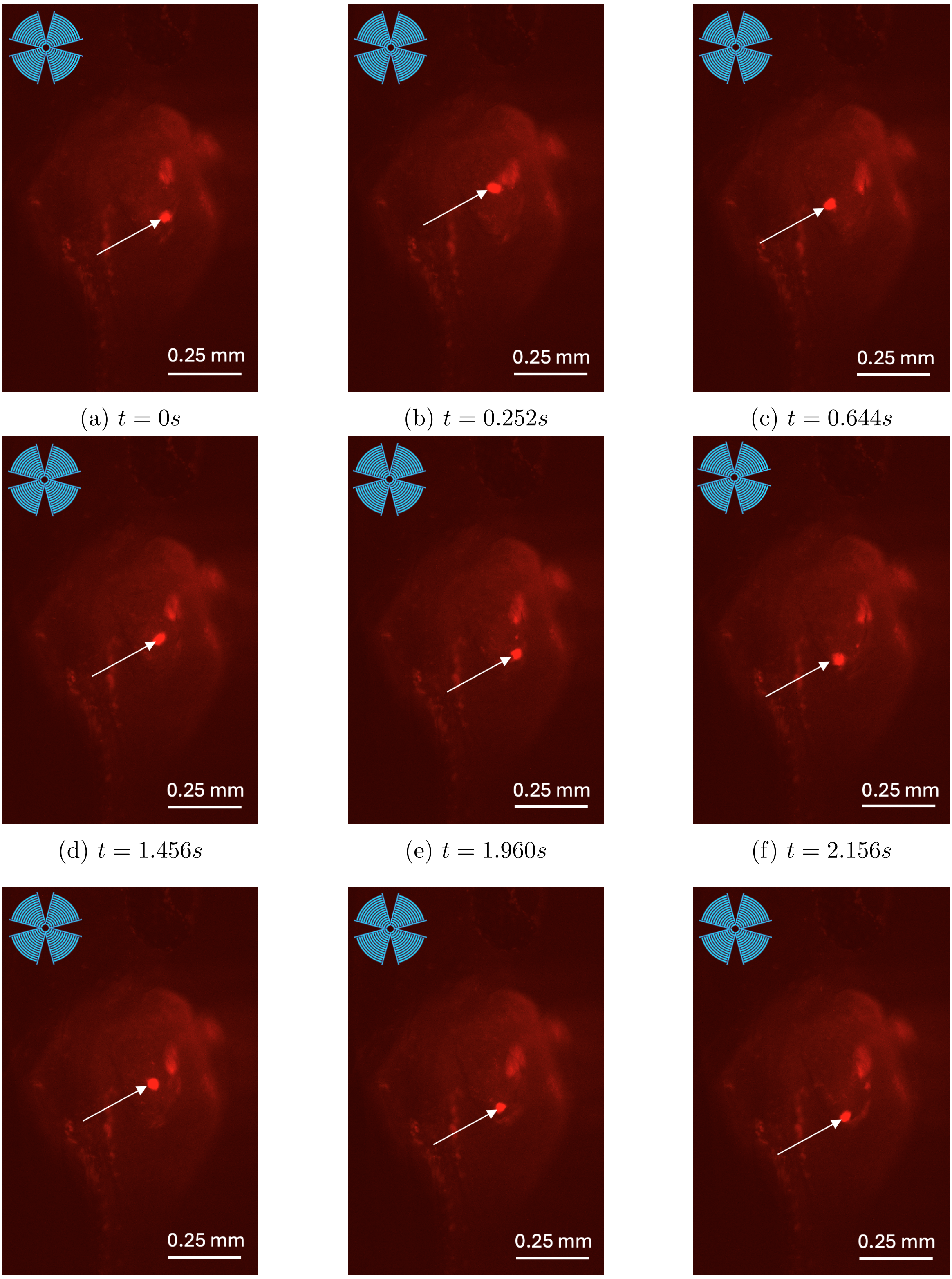

(a) $t = 0s$ (b) $t = 0.252s$ (c) $t = 0.644s$

(d) $t = 1.456s$ (e) $t = 1.960s$ (f) $t = 2.156s$

(g) $t = 3.360s$ (h) $t = 3.892s$ (i) $t = 5.208s$

Figure A.4: Manipulation of red fluorescent microbubbles in the yolk sac of a zebrafish embryo using the FIDT with a resonance frequency of approximately 59.3 MHz.